Preparation of TRU alloys by electrochemical or lithium reduction method

Kunihisa Nakajima,[1] **Takashi Iwai,**[1] **Yasuo Arai,**[1] **Masaki Kurata,**[2] **Kinya Nakamura,**[2] **Yuji Arita**[3]
[1]Japan Atomic Energy Agency
[2]Central Research Institute of Electric Power Industry
[3]Nagoya University

Abstract

Information on phase diagram and thermodynamic data of transuranium (TRU) alloys are required for the development of metallic fuel fabrication technology and fuel design for TRU transmutation. Metallic samples containing TRU elements such as Np, Pu and Am were prepared by electrochemical or lithium (Li) reduction of their oxides. In the present study, the electrochemical reduction of mixed-oxide lumps with the nominal composition of $(U_{0.61}Np_{0.10}Pu_{0.29})O_2$ *was performed in molten lithium chloride (LiCl) electrolyte at 923 K. It was found from the cross-sectional observation of the sample that the mixed-oxide was almost completely reduced. In the case of* PuO_2*, however, the electrochemical reduction did not progress inside the sample since a dense metal skin covered the sample surface. So mixed-oxides with high TRU contents were reduced with Li metal in LiCl melt. At first,* UO_2*,* NpO_2 *and* PuO_2 *containing 10 at.%* AmO_2 *powders were mixed with an agate mortar and then the mixture of mixed-oxide powders, Li metal and LiCl were heated and stirred at ~973 K. After removing LiCl solvent including* Li_2O *generated by the reduction, the metallic samples were arc-melted for homogenisation. These alloys were annealed at 923 K or 791 K in eutectic LiCl and potassium chloride (KCl) molten salt and quenched. These anneal-quenched samples were used for the thermal analyses and the microstructural observations.*

Introduction

Metallic fuel core is expected to yield high actinide burning rate owing to an extremely hard neutron spectrum. Metallic fuel is, therefore, a promising fuel for transmutation of transuranium elements (TRU). For the development of transmutation technology by use of a metallic fuel, it is necessary to establish a basic concept such as a fuel design, a core design and a fuel fabrication method. As for the fuel design, it is important to understand the thermodynamic properties of TRU alloys relevant to their phase stabilities. In the case of R&D on U-Pu-Zr based metallic fuel containing up to 5 at.% of minor actinides, it is expected that mechanical property and thermal conductivity of the TRU metallic fuel do not significantly differ from those of the U-Pu-Zr fuel [1]. On the other hand, the phase stability data, which are required for evaluation of melting temperature, compatibility with a cladding tube and redistribution of fuel constituents, have not been well established and should be obtained from experimental examinations. In this study, TRU alloy samples used for experimental examinations were prepared from their oxides.

For the reduction of TRU oxides to their metals, the electrochemical reduction [2-5] and the lithium (Li) reduction methods [6-8] were employed in this study. The electrochemical reduction method was applied to preparation of the samples with comparatively low TRU contents. While the Li reduction method was applied to the samples containing high Np and Pu contents, which have low melting point. Electrochemical reduction method is the technique to reduce oxides into their metals directly by electrochemical diffusion of oxygen ions from an oxide cathode to an anode through lithium chloride (LiCl) melt. It has been reported that about 0.9 g mixed-oxide pellet pieces with the composition of $(U_{0.55}Pu_{0.40}Np_{0.05})O_2$ can be successfully reduced to metal by this method [3]. In this study, the same method is applied to the reduction of TRU oxides. On the other hand, in the Li reduction method, Li metal and LiCl melt are used as a reductant and a solvent for conversion of actinide oxides to metal, respectively. Li oxide (Li_2O) generated as a by-product in the Li reduction would dissolve into the LiCl melt. After the conversion of oxide to metal, these reduced products were separated from the molten salt and arc-melted to be homogenised in this study.

This report concerns the results of preparation of TRU alloy samples, which were used for metallographic observation, electron microprobe analysis and thermal property measurements.

Experimental

All the experiments were carried out in high-purity argon atmosphere glove boxes. Both the oxygen and moisture contents were kept less than a few ppm.

Preparation of mixed-oxide pellets for electrochemical reduction

Low density MOX pellets are favourable for electrochemical reduction as starting materials since molten salt electrolyte easily permeates inside the pellets during the electrochemical reduction. So the mixture of UO_2, NpO_2 and PuO_2 powders were pressed into green pellets and heated at 1 770 K in Ar-H_2 gas for 1 hr. In this procedure, oxide pellets with 60-80% of theoretical density were obtained. The nominal compositions of these mixed-oxide pellets prepared in this study are $(U_{0.71}Pu_{0.29})O_2$, $(U_{0.42}Pu_{0.58})O_2$ and $(U_{0.61} Np_{0.10}Pu_{0.29})O_2$. As for the electrochemical reduction of $(U_{0.71}Pu_{0.29})O_2$, a few grams of pellet was reduced to metal for investigation of the phase relation in the system of U-29Pu. The phase relation in the temperature range of 800-900 K reported in the past is hard to understand thermodynamically. As for the electrochemical reduction of $(U_{0.42}Pu_{0.58})O_2$, successful conversion to its metal ingot with 10 g scale has been reported [5]. In the present study, the electrochemical reduction of the same compositional MOX pellet was carried out to utilise as the mother alloy required for preparation of TRU alloys with various kinds of composition. As for the electrochemical reduction of $(U_{0.61}Np_{0.10}Pu_{0.29})O_2$, the composition was selected from preliminary analyses using thermodynamic database of TRU alloys.

Preparation of mixed-oxides for Li reduction

PuO_2 powder used for the Li reduction contained about 10 at.% AmO_2 and 2 wt.% fluorine. It has been reported that heat treatment at 1 970 K could reduce the fluorine content to a few tens of ppm in the oxide samples [9]. Thus, the PuO_2 powder was heated at 1 273 K in air and then at 1 970 K in Ar-H_2 mixed gas to remove the fluorine completely. Actually, the weight loss of the PuO_2 sample was found to be 2.9%. Most fluorine in the PuO_2 powder would evaporate. While UO_2 and NpO_2 samples were heated at 1 073 K in Ar-H_2 gas and air, respectively, to remove absorption gas and water in the samples and to control their stoichiometry. These TRU dioxide powders used for the Li reduction were mixed in an agate mortar with the compositions indicated in Table 1. These compositions were selected based on preliminary thermodynamic analyses.

Table 1: Experimental conditions of the Li reduction

Sample (at.%)*	Amount of mixed-oxide (mg)	Amount of Li metal (mg)	Amount of LiCl (g)
Pu-9.5Am	512	79.5	2.19
U-64Pu-6.7Am	398	46.8	0.973
U-43Pu-4.6Am	406	47.3	1.00
U-22Pu-2.4Am	420	62.5	1.06
U-60Np	283	51.4	1.07
Np-45Pu-4.8Am	252	62.5	1.03

* Nominal composition.

Electrochemical reduction procedure

EG&G Princeton Applied Research potentio/galvanostat Model 273A and EG&G 270/250 Research Electrochemistry Software were used for the electrochemical reduction. Electrochemical reduction was performed at 923 K by use of molten LiCl electrolyte with about 1 wt.% concentration of Li_2O, which acted as a carrier of oxygen ion. Pt wire (1 mm diameter) or Pt sheet and Pb-32 at.% Li alloy were used as an anode and a reference electrodes, respectively. At the cathode, mixed-oxide pellets were loaded into a basket made from Ta mesh (40 mesh) and reduced to metal electrochemically. A small electrolytic cell with an inner diameter of 50 mm and 100 g molten salt were used. Components of the apparatus immersed with the molten salt such as an electrolytic cell and electrode tubes were made of magnesia (MG-12; Nikkato Co.). Prior to the electrochemical reduction of a mixed-oxide, cyclic voltammetry was carried out in the same LiCl-Li_2O system. The same cyclic voltammogram pattern as the previous result was observed [4]. A reduction electric current rose in the vicinity of -0.5 V, corresponding to the reduction of lithium ($Li^+ + e^- = Li$). When the potential moved back to the rest potential, the current due to the dissolution of deposited Li metal was observed. Pt is the anode material for the electrochemical reduction tests and the potential was scanned to the higher potential to check anodic reactions. Two anodic current peaks appeared. One peak was observed at near 1.9 V and another was at 2.1 V. According to the previous results, these two peaks were considered to correspond to the formation of Li_2PtO_3 and the oxidation of O^{2-} evolving O_2, respectively [4]. The redox potential of the Li^+/Li couple is about -0.5 V. So the difference between the potentials of these two anodic peaks and the Li redox potential became 2.4 V and 2.6 V, respectively. The latter value agreed with that reported in the past [5]. Sakamura, *et al*. reported that Pt electrode eroded due to the formation of Li_2PtO_3 and the anodic dissolution of Pt [4]. They recommended that the anodic potential should be controlled in the range of 2.8-3.2 V versus the redox potential of Li^+/Li where the oxygen generated predominantly. This condition is effective to suppress the corrosion of Pt electrode. In the present study, the electrochemical reduction was carried out within the anode potential of 2.3-2.7 V versus the reference electrode of Pb-32 at.% Li alloy.

Li reduction procedure

Mixed-oxide powders were put into a crucible where Li metal was spread over the bottom of crucible and then the LiCl was added to the crucible. The crucible ($\varphi16 \times \varphi14 \times 20$H) was made of Y_2O_3 (Y2O3-B; Nikkato Co.). The sample was heated up to 973 K and then stirred at 100 rpm for 30 min. with a Mo stirrer of 5 mm diameter, the tip of which was cut obliquely. The experimental conditions in the Li reduction method are shown in Table 1. The amount of LiCl was determined from the solubility of Li_2O, which was higher than 10 wt.% at 973 K [8].

Distillation of molten salt

Molten salt electrolyte accompanied with the reduced products should be removed. Since the vapour pressure of LiCl is about 3 kPa at 1 273 K molten salt can be distillated in a vacuum. Kato, *et al.* recommended that, prior to the distillation of molten salt electrolyte, another LiCl should be added to the sample and re-heated to change the porous reduced product into dense metal ingot [8]. These procedures are effective to prevent the reduced product from exposure to an ambient oxidising atmosphere because of the reduced sample surface area. So the reduced product was covered with an additional LiCl and heated at temperatures higher than its melting temperature for 1 hr under atmospheric pressure. Then, the molten salt was distilled in a vacuum.

Arc melting

Titanium metal was used as an oxygen getter. Arc melting was used to alloy the reduced products with Zr. So each ingot was turned over and re-melted several times to be homogenised. However, TRU mother alloys (U-29Pu, U-58Pu and U-10Np-29Pu alloys) were also arc-melted since they did not melt and agglomerate in the distillation process.

Results and discussion

Samples prepared in the electrochemical reduction method

It was found from cyclic voltammograms of $(U_{0.71}Pu_{0.29})O_2$ that both the reduction and the dissolution currents increased with increasing amounts of samples. Figure 1 shows change of the cathode potential of $(U_{0.42}Pu_{0.58})O_2$ during the electrochemical reduction. Although the potential was not stable in the beginning of the electrolysis, the reduction of oxide proceeded at the stable potential in the end. The potential during the electrolysis was obviously lower than -0.5 V corresponding to the redox potential of Li, which was attributed to the IR drop. In the end of the electrolysis, the cathodic potential gradually decreased and settled down to a constant value. When the electrolysis stopped in this state, the rest potential indicated the redox potential of Li^+/Li couple, which suggested that the deposited Li metal occurred. So it is considered that the reduction rate of oxide gradually decreased and the electric current was supplied from the reduction of Li^+ in the molten salt instead of the

Figure 1: Change of the cathode potential during the electrochemical reduction of $(U_{0.42}Pu_{0.58})O_2$

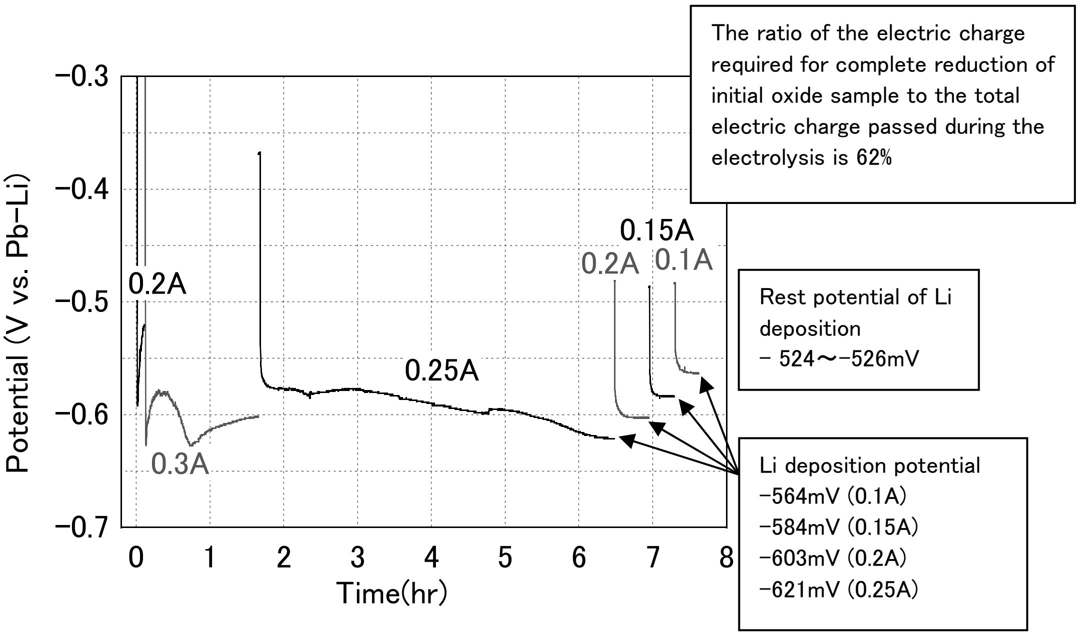

The ratio of the electric charge required for complete reduction of initial oxide sample to the total electric charge passed during the electrolysis is 62%

Rest potential of Li deposition
− 524〜−526mV

Li deposition potential
−564mV (0.1A)
−584mV (0.15A)
−603mV (0.2A)
−621mV (0.25A)

reduction of oxide. Thus, the electric current was decreased stepwise to avoid the massive Li metal deposition. Figure 2 shows cross-sections of the reduced product $(U_{0.71}Pu_{0.29})O_2$ and $(U_{0.61}Np_{0.10}Pu_{0.29})O_2$. The electrochemical reduction of these two samples was interrupted to see how the reduction progressed. The electrolysis of the former sample was interrupted on the condition that the ratio of the electric charge theoretically required for complete reduction of initial oxide sample to the total electric charge passed during the electrolysis is 85%. The latter case is 123%. As shown in this figure, a non-reduced oxide remained in the central part of the reduced product. So it was found that the reduction progressed from the surface to the centre of oxide pellet. Figure 3 shows appearances of the whole sample after the electrochemical reduction of $(U_{0.61}Np_{0.10}Pu_{0.29})O_2$ and a cross-section of a reduced product. It was found from the cross-section of the reduced products that the mixed-oxide was almost completely reduced.

Figure 2: Cross-sections of the reduced product $(U_{0.71}Pu_{0.29})O_2$ and $(U_{0.61}Np_{0.10}Pu_{0.29})O_2$ after the interruption of the electrochemical reductions on the conditions described in the text

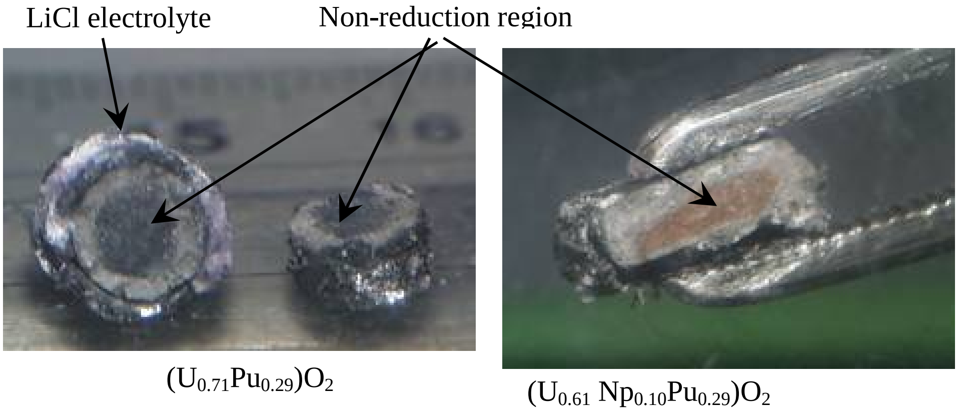

Figure 3: Appearances of: a) the cathode after the electrochemical reduction of $(U_{0.61}Np_{0.10}Pu_{0.29})O_2$, b) the entire reduced sample and c) a cross-section of the reduced piece

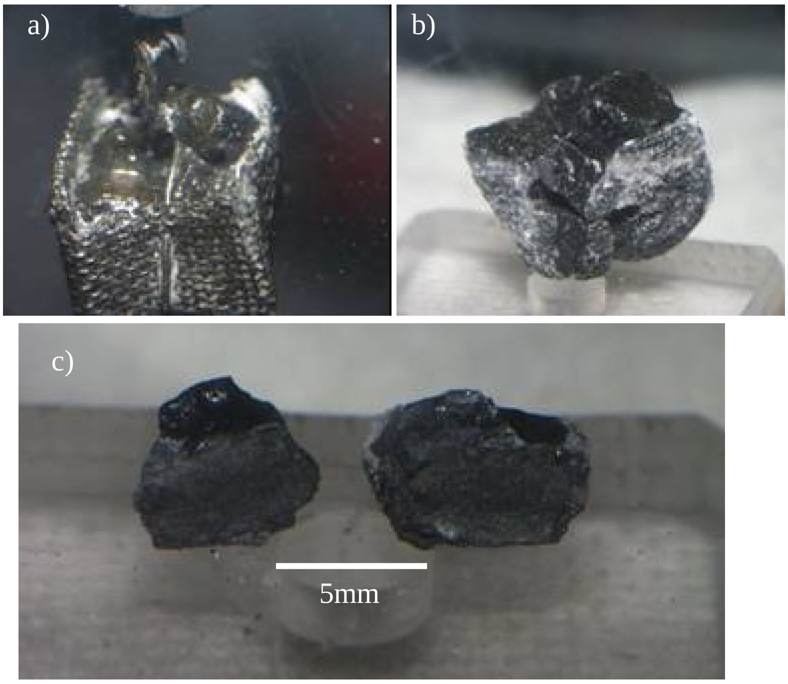

Since the molten salt penetrated inside the reduced products it was distilled in vacuum. The appearance of the TRU alloy (U-10Np-29Pu) after the vacuum distillation is shown in Figure 4. These alloy pieces were found to be considerably rusted and partially crumbled. Table 2 shows the sample weights of TRU alloys after the vacuum distillation together with the metal element contents in the starting material used for the electrochemical reduction. The weight of the metal contents was calculated from that of the starting mixed-oxide sample. As shown in this table, weights of these samples recovered from the vacuum distillation process were in good agreement with those of the starting samples. So good material balance was realised through the electrochemical reduction and vacuum distillation processes.

Figure 4: Appearance of U-10Np-29Pu (4.121 g) after the vacuum distillation

Table 2: Results of the material balances during the electrochemical and Li reduction processes

Sample (at.%) [a]	Metal element content in MOX (mg)	Sample weight after the vacuum distillation (mg)	Sample weight after the arc melting (mg)	Yield efficiency (%)
U-58Pu[b]	2 681	2 646	2 588	96.5
U-10Np-29Pu[b]	4 099	4 121	3 723	90.8
U-64Pu-6.7Am[c]	351	312	272	77
U-43Pu-4.6Am[c]	358	357	335	94
U-22Pu-2.4Am[c]	370	–	414	112
U-60Np[c]	303	298	290	96
Np-45Pu-4.8Am[c]	356	–	291	82

[a] Nominal composition.

[b] Samples prepared in the electrochemical reduction.

[c] Samples prepared in the Li reduction.

Figure 5 shows appearances of U-10Np-29Pu after the arc melting. As shown in this figure, a considerable amount of soot around the sample was generated during the arc melting. The occurrence of this soot might be related to the potential oxide scale on the surface of the sample after the distillation process as shown in Figure 4. Further, a red arc discharge resulting from flame reaction of alkaline metal was also observed during the arc melting. So it was considered that the molten salt was not completely removed in the vacuum distillation process. Table 2 also shows the yield efficiencies calculated from the weight of buttons of TRU alloys after the arc melting. It was found that the overall yield efficiencies attained to be higher than 90%. Since the soot also generated during the arc melting of the other mother alloys, the amount of loss of Pu could not be evaluated from the weight difference of the sample before and after the arc melting. Table 3 summarises the results of the weight loss of the arc-melted alloys. It was found that there were the significant differences of the weight loss among the alloy samples. Actually, it took a long time for some samples to be agglomerated and alloyed with Zr metal by arc melting. So these differences must depend on the arc-melting time. Namely some samples were suggested to evaporate significantly during the arc melting.

Figure 5: Appearances of U-10Np-29Pu (3.723 g) after the arc melting

Table 3: Results of the weight loss of the arc-melted alloys

Sample (at.%)[a]	Sample weight (mg)	Weight loss (mg)	Weight loss ratio (%)
U-55Pu-5Zr	438	34	7.3
U-10Np-29Pu-3Zr	283	12	4.1
U-9Np-27Pu-10Zr	348	1.2	0.3
U-4Np-13Pu-4Zr	494	0.8	0.2
U-7Np-34Pu-8Zr	306	4.4	1.4
U-4Np-44Pu-4Zr	370	51	12

[a] Nominal composition.

At first, mixed-oxides with high TRU contents were also planned to be reduced electrochemically. However, it was found in the electrochemical reduction of PuO_2 that only the sample surface could be reduced to metal. Figure 6 shows appearances of the sample after the vacuum distillation. Half of this sample was pulverised in an agate mortar and it was found that there existed ductile substances as well as powders as shown in this figure. This powder was identified to be a hexagonal Pu_2O_3 by X-ray diffractometry. As one of the reasons why only the sample surface of PuO_2 was converted to metal, Pu metal had low melting temperature (913 K) and the reduced Pu metal on the sample surface might cover the opening pore and blocked the penetration pass of the molten salt electrolyte which acted as a carrier of oxygen ions. It is, therefore, considered that the existence of the opening pore in the oxide pellets is essential for the continuous electrolysis. Thus, the samples with high Np and Pu contents were reduced to metal by the Li reduction method.

Samples prepared in the Li reduction method

Since the reduced product sunk to the bottom of the crucible after the Li reduction, the crucible was turned over and heated upside down to remove the molten salt. The crucible was covered with Ta mesh for the reduced product not to drop together with the molten salt. The most amount of molten salt was dropped off the crucible. Figure 7 shows appearances of the Pu-9.5Am sample after the melting drop of the molten salt. Furthermore, the molten salt accompanied with the reduced product was completely removed by vacuum distillation in the temperature range of 1 070-1 420 K for 1 hr. The reduced products except the Pu-9.5Am sample were also arc-melted for a few dozen to a few hundred seconds to agglomerate and homogenise. Figure 8 shows appearances of the TRU alloy samples after the arc melting. Table 2 also shows results of the yield efficiencies calculated from the sample weight. As shown in this table, there seems no significant loss until the vacuum distillation process. But the weight loss of samples with high Am and Pu contents obviously occurred after the arc melting. This weight reduction suggested a significant loss of Am and Pu, which have relatively high vapour pressures.

Figure 6: Appearances of the sample after the electrochemical reduction and the vacuum distillation of PuO_2

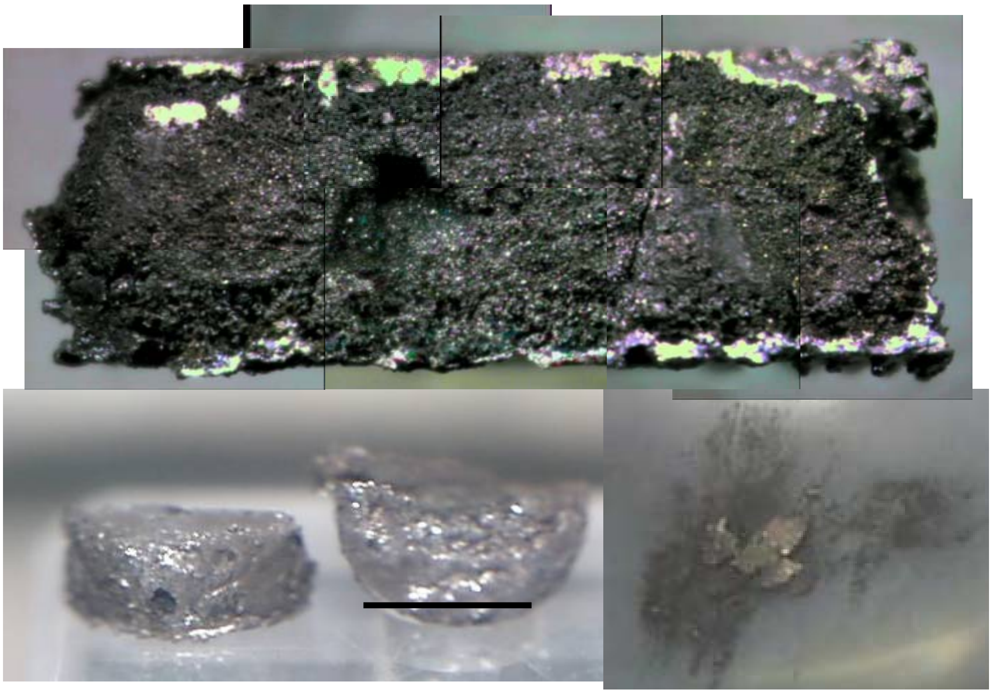

Figure 7: Appearances of the Pu-9.5Am sample after the melting drop of the molten salt

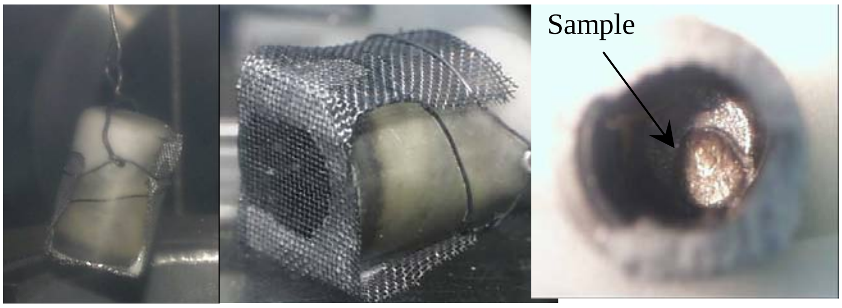

Figure 8: Appearances of the TRU alloys after the arc melting

U-64Pu-6.7Am

U-60Np

Np-45Pu-4.8Am

Summary

A few grams of mother alloys containing TRU elements were prepared from their mixed-oxides in the electrochemical reduction method. However, it was found in the electrochemical reduction of PuO_2 that only the sample surface could be reduced to metal. It is anticipated that electrochemical conversion of mixed-oxides with high Np and Pu contents into metals are difficult owing to production of low-melting metals. In the present study, the Li reduction method was applied to the reduction of these TRU oxides and the alloys with high TRU contents were prepared.

Acknowledgements

The present study is the result of "Development of a Fabrication Technology of TRU Alloy Fuel and Fuel Design for TRU Transmutation" entrusted to Nagoya University by the Ministry of Education, Culture, Sports, Science and Technology of Japan (MEXT).

References

[1] Kurata, M., *et al.*, *Development of Transmutation Technology of Long-lived Nuclides – Properties of the Alloy Including MA and RE*, CRIEPI Report No.T92005 (1992) (in Japanese).

[2] Chen, G.Z., D.J. Fray, T.W. Farthing, "Direct Electrochemical Reduction of Titanium Dioxide to Titanium in Molten Calcium Chloride", *Nature*, 407, 361 (2000).

[3] Iizuka, M., Y. Sakamura, T. Inoue, "Electrochemical Reduction of (U-40Pu-5Np)O_2 in Molten LiCl Electrolyte", *J. Nucl. Mater.*, 359, 102 (2006).

[4] Sakamura, Y., M. Kurata, T. Inoue, "Electrochemical Reduction of UO_2 in Molten $CaCl_2$ or LiCl", *J. Electrochem. Soc.*, 153 (3), D31 (2006).

[5] Kato, T., *et al.*, *Development of Metal Fuel Fabrication Technology for Irradiation Test in JOYO – Production of Uranium-plutonium Alloy by Electrochemical Reduction*, CRIEPI report L05010 (2006) (in Japanese).

[6] Usami, T., *et al.*, "Lithium Reduction of a MOX Pellet", *J. Nucl. Sci. Technol.*, Supplement 3, 858 (2001).

[7] Usami, T., *et al.*, "Applicability of the Lithium Reduction Process to Transuranium Elements", *Proc. of GLOBAL 2001*, FP164.pdf (2001).

[8] Usami, T., *et al.*, "Pyrochemical Reduction of Uranium Dioxide and Plutonium Dioxide by Lithium Metal", *J. Nucl. Mater.* 300, 15 (2002).

[9] Ozaki, Y., *et al.*, *Evaluation of Remaining Behavior of Halogen on the Fabrication of MOX Pellet Containing Am*, JNC TN 9400 2004-070 (2004).

Thermal conductivities of neptunium and americium mononitrides

Tsuyoshi Nishi, Masahide Takano, Akinori Itoh, Mitsuo Akabori, Yasuo Arai, Kazuo Minato
Nuclear Science and Engineering Directorate
Japan Atomic Energy Agency

Abstract

Nitride has several advantages as the fuel materials for transmutation of minor actinides (MA). However, thermal property database of the nitride fuel has not been well established, especially for MA nitrides. In this study, neptunium nitride (NpN) and americium nitride (AmN) were prepared by carbothermic reduction of the respective dioxides. The thermal diffusivities of NpN and AmN were measured using a laser flash method. The heat capacities of NpN and AmN were determined with the drop calorimetry. The thermal diffusivity of NpN tends to remain unchanged with increasing temperature in the temperature range 473 to 1 473 K, and that of AmN tends to slightly decrease with increasing temperature in the same temperature range. The heat capacity of NpN obtained was close to those of UN and PuN, while that of AmN was slightly smaller than those of UN, NpN and PuN. The thermal conductivities of NpN and AmN were determined from the measured thermal diffusivities, heat capacities and bulk densities. It was found that the thermal conductivities of NpN and AmN slightly increased with temperature in the temperature range investigated.

Introduction

The long-term hazard of radioactive wastes arising from nuclear energy production is a matter of discussion and public concern. To reduce the radiotoxicity of the high-level waste and use the repository efficiently, the partitioning and transmutation of minor actinides (MA: Np, Am, Cm) as well as multi-recycle of plutonium is an option for the future nuclear fuel cycle. Many concepts have been proposed on the fuels together with advanced reactors or accelerator-driven systems (ADS). Among various fuel types, nitride fuel is one of the candidates for the MA-bearing fuels because of the high melting points, good thermal conductivities and mutual solubility.

Thermal conductivities of MA nitrides are fundamental thermophysical properties for the design of MA-bearing fuels and analysis of their behavior [1-4]. Some results have been reported for the thermal conductivities of UN, NpN, PuN and the solid solution of (U,Pu)N, (U,Np)N and (Np,Pu)N [5-7].

Recently, experimental data for the thermal conductivity of AmN were obtained [8]. But, the thermal conductivity of AmN was obtained by use of the heat capacity of PuN in literature [9].

In this study, the thermal conductivities of NpN and AmN were evaluated from the measured thermal diffusivities, heat capacities and bulk densities. The thermal diffusivities and heat capacities were determined by using a laser flash method and a drop calorimetry, respectively.

Experimental

Samples

The NpN and AmN samples were prepared by the carbothermic reduction of the respective dioxides $^{237}NpO_2$ and $^{243}AmO_2$; characteristics of the $^{237}NpO_2$ and $^{243}AmO_2$ powders are described elsewhere [8,10]. Each powder was mixed with carbon powder. The mixtures were compacted and heated at 1 573-1 693 K in flowing N_2 gas at 500 ml/min. After the CO gas release measured by use of an infrared spectrometer subsided, the atmosphere gas was replaced by flowing $N_2 + 4\%H_2$ mixed gas to remove the residual carbon. The additional heating was continued at 1 793 K until the CO gas release subsided again. The products of carbothermic reduction were ground and pressed to disks. The NpN and AmN disks were sintered at 2 023 K and 1 823-1 893 K in flowing $N_2 + 4\%H_2$ gas, respectively. Characteristics of NpN and AmN samples are summarised in Table 1. The oxygen and nitrogen contents were measured with an apparatus (HORIBA, EMGA-550) based on the inert gas fusion technique. The carbon content was measured with an apparatus (CE Instruments, NC-2500) based on the combustion technique.

Table 1: Characteristics of NpN and AmN samples

	NpN	AmN	
		For thermal diffusivity measurements	For heat capacity measurements
Nitrogen (wt.%)	5.48±0.10	5.13±0.10	4.96±0.10
Oxygen (wt.%)	0.32±0.15	0.55±0.10	1.22±0.10
Carbon (wt.%)	≦0.05	0.08±0.10	0.21±0.10

Thermal diffusivity and heat capacity measurements

The thermal diffusivity was measured by the laser flash apparatus installed in the glove box with a highly-purified argon gas atmosphere. In the glove box, the oxygen and moisture contents were controlled less than 2 and 3 ppm, respectively, in order to handle MA nitride samples which are unstable in the air. The sample was set in the sample holder applied to the vertical type laser flash apparatus and heated to the desired temperature with a Mo heater. The thermal diffusivity measurements were performed from 473 to 1 473 K in vacuum with background pressure of less than 2.5×10^{-4} Pa.

The thermal diffusivity was determined from the temperature rise at the rear surface of the sample measured with an InSb infrared detector after the front surface of the sample was instantaneously irradiated by a pulse of Nd glass laser. The data of temperature response curve at the rear surface was analysed by the curve fitting method [11,12]. It was elucidated that the uncertainty of the thermal diffusivity values obtained with this system was estimated to be less than 5% in comparison with literature values [13].

On the other hand, the enthalpy increment of NpN and AmN was measured using a twin-type drop calorimeter (SETARAM, HT-1000) in the glove box [14]. The apparatus consisted of two differential calorimetric units located in two cylindrical wells. The temperature difference between two calorimetric units was detected by Pt-Pt10%Rh thermocouples.

The samples for enthalpy increment measurements were loaded in the platinum containers. The weights of NpN and AmN samples for enthalpy increment measurements are summarised in Table 2. The container was evacuated and sealed in argon gas atmosphere in the background pressure of about 10 kPa. The sapphire was also sealed in another container as the standard sample. The enthalpy increment of “blank” Pt container without any sample was also measured.

Table 2: The weights of NpN and AmN samples for enthalpy increment measurements

	NpN	AmN
Weight (mg)	102.06	42.09
Pt container weight (mg)	521.58	373.93

The sample enclosed with the container was kept at room temperature for at least one hour in a polyethylene container placed above the calorimeter to assure the thermal equilibrium. The room temperature, which was measured with the thermometer placed in the polyethylene container, was within a range from 297 to 305 K. Then the sample was dropped into the calorimeter kept at a constant temperature. The heat flows of the samples Q were calculated by subtracting those of the Pt containers from those of the samples enclosed with the Pt containers. The heat flow Q is determined as Q = Aq, where A is the correction coefficient of the calorimeter and q is the non-corrected heat flow. The correction coefficient was determined as the ratio between recommended heat flow per weight of sapphire $Q\text{-}Q_{298.15}$ [15] and experimental one of this study in the temperature range from 312 to 1 121 K.

The enthalpy increments of samples were obtained by multiplying the heat flow of samples by respective formula weights. The enthalpy increment $H\text{-}H_{298.15}$ values at various temperatures were well fitted to quadratic polynomial expression in temperature T:

$$H\text{-}H_{298.15} = a\,T^2 + b\,T + c \tag{1}$$

Since the room temperature (RT) was not constant, each $H\text{-}H_{298.15}$ value was obtained by subtracting $H_{298.15}\text{-}H_{RT}$ values from $H\text{-}H_{RT}$ values. The heat capacity was obtained from the derivative of Eq. (1) with respect to temperature and is given by:

$$C_p = 2a\,T + b \tag{2}$$

The measured thermal conductivities corrected to theoretical densities were estimated. The thermal conductivity, λ, can be obtained by the following equation:

$$\lambda = \alpha C_p \rho \tag{3}$$

where C_p is the heat capacity and ρ is the bulk density of the sample. In order to estimate the thermal conductivities with theoretical densities, the present data were corrected by the analytical equation of Schulz [16]:

$$\lambda = \lambda_{TD}(1 - P)x \tag{4}$$

where λ_{TD} is the thermal conductivity of the sample with theoretical density, P is the porosity of the sample and x = 1.5 is the parameter for closed pores of spherical shape. Among a variety of porosity correction formulas, Eq. (4) was in best agreement with the result of the finite element computations in the wide range of the porosity up to 0.3 as reported by Bakker, *et al.* [17].

Results and discussion

Bulk density

The bulk densities of the sintered NpN and AmN samples for thermal diffusivity measurements were calculated from the diameter, thickness and weight to be 11.33 and 10.56 Mg/m^3, respectively. The diameter and thickness of the sintered samples were measured by a dial gauge to be 2.951 and 1.772 mm for NpN and to be 3.039 and 0.644 mm for AmN, respectively. The weights of the sintered NpN and AmN samples were measured by an electronic balance to be 137.30 mg and 49.34 mg, respectively. After the thermal diffusivity measurements, the NpN and AmN samples were examined by powder X-ray diffraction analysis to determine the lattice parameter. The lattice parameters of NpN and AmN were determined to be 0.4893 and 0.5003 nm, respectively. The theoretical densities of NpN and AmN were calculated from the atomic weight and lattice parameter to be 14.23 Mg/m^3 and to be 13.62 Mg/m^3, respectively. Thus, the relative densities of the sintered NpN and AmN samples for thermal diffusivity measurements corresponded to 79.6%TD (TD: theoretical density) and 77.5%TD, respectively.

Thermal diffusivity

The thermal diffusivity measurements were performed in both heating and cooling processes. The measured thermal diffusivities are shown in Figure 1. It was found that good reproducibility of the experimental thermal diffusivity data was confirmed by the heating and cooling measurements. The deviation of thermal diffusivities obtained in both heating and cooling processes was within 5%. As shown in Figure 1, the thermal diffusivity of NpN tends to remain unchanged and that of AmN tends to slightly decrease with increasing temperature from 473 to 1 473 K.

Figure 1: Thermal diffusivities of NpN and AmN

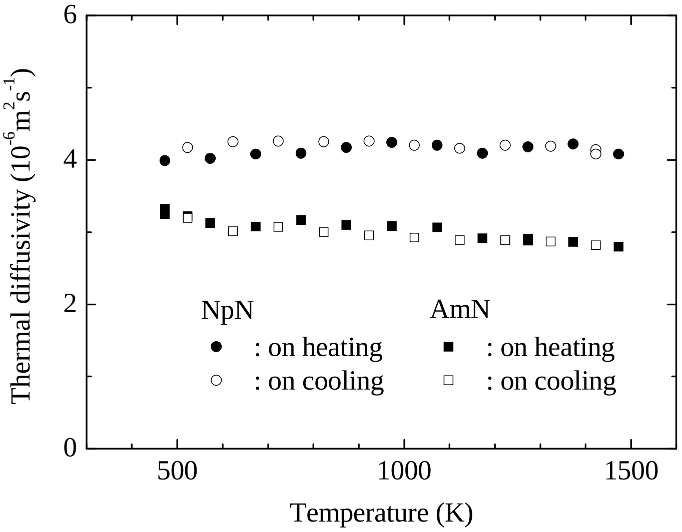

Heat capacity

Figure 2 shows the enthalpy increments of NpN and AmN. No thermal anomalies were observed. The experimental data of NpN and AmN were fitted to quadratic polynomial equation using the least squares method. The result for NpN is:

$$H\text{-}H_{298.15}\ (\text{kJmol}^{-1}) = 9.358 \times 10^{-6}\ T^2 + 0.04275\ T - 13.63 \quad (5)$$

for the temperature range from 334 to 1 067 K and the result for AmN is:

$$H\text{-}H_{298.15}\ (\text{kJmol}^{-1}) = 7.816 \times 10^{-6}\ T^2 + 0.04244\ T - 14.09 \quad (6)$$

for the temperature range from 354 to 1 071 K. The uncertainties of the heat capacities for NpN and AmN ascribed to the statistical error of the enthalpy increments were ±3.2% and ±7.0% respectively.

The heat capacities of NpN and AmN were first derivative of Eqs. (5) and (6) with respect to temperature. The heat capacities of NpN and AmN obtained are expressed by:

$$C_p\ (\mathrm{Jmol^{-1}K^{-1}}) = 1.872 \times 10^{-2}\ T + 42.75 \tag{7}$$

$$C_p\ (\mathrm{Jmol^{-1}K^{-1}}) = 1.563 \times 10^{-2}\ T + 42.44 \tag{8}$$

and shown in Figure 3, together with those of UN [18] and PuN [9]. The heat capacity of NpN obtained was in good agreement with the reported values [19] in the temperature range from 334 to 1 067 K. The heat capacity of NpN was close to those of UN and PuN. On the other hand, that of AmN was slightly smaller than those of UN, NpN and PuN in the temperature range investigated. However, considering the uncertainty of the heat capacity, it is seen that actinide nitrides have similar heat capacities with similar temperature dependence.

Figure 2: Enthalpy increment $H\text{-}H_{298.15}$ values of NpN and AmN

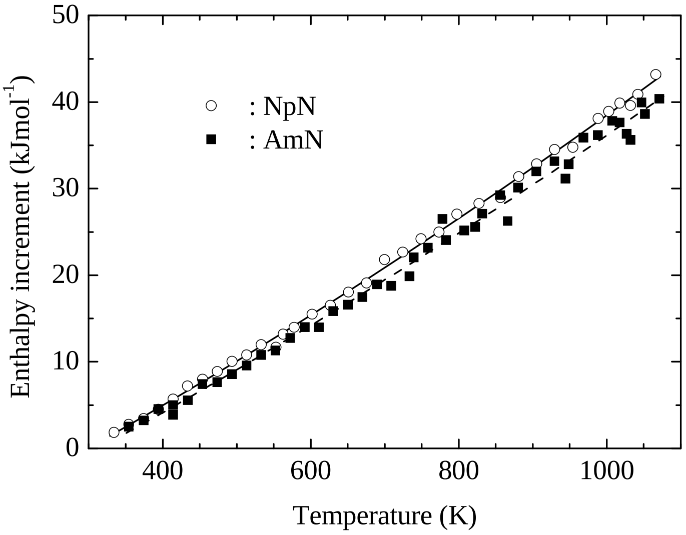

Figure 3: Heat capacities of NpN and AmN together with those of UN [18] and PuN [9]

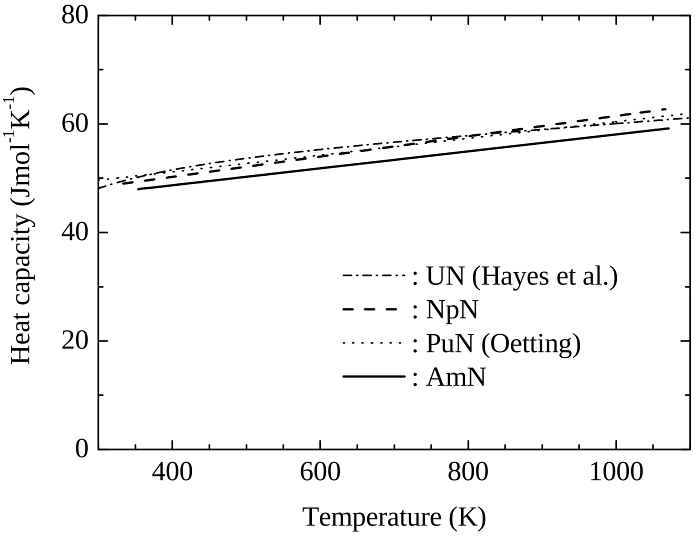

Thermal conductivity

The thermal conductivities of NpN and AmN corrected to theoretical densities are shown in Figure 4, together with those of UN, PuN [5] and UO_2 [20]. The heat capacity of NpN from 1 067 to 1 473 K and that of AmN from 1 071 to 1 473 K were not measured in the present study, unfortunately. Thus, to estimate the thermal conductivity, the heat capacity of NpN from 1 067 to 1 473 K and that of AmN from 1 071 to 1 473 K were calculated by simply extrapolating Eqs. (7) and (8). The fitted results of the thermal conductivity for NpN is:

$$\lambda(\mathrm{Wm^{-1}K^{-1}}) = -1.98 \times 10^{-6}\ T^2 + 0.00890\ T + 9.53 \tag{9}$$

and the result for AmN is:

$$\lambda(\mathrm{Wm^{-1}K^{-1}}) = -2.54 \times 10^{-8}\ T^2 + 0.00147\ T + 8.99 \tag{10}$$

in the temperature range from 473 to 1 473 K.

Figure 4: Estimated thermal conductivities of NpN and AmN with theoretical densities (solid lines), together with those for UN, PuN (broken lines) and UO_2 (dotted line)

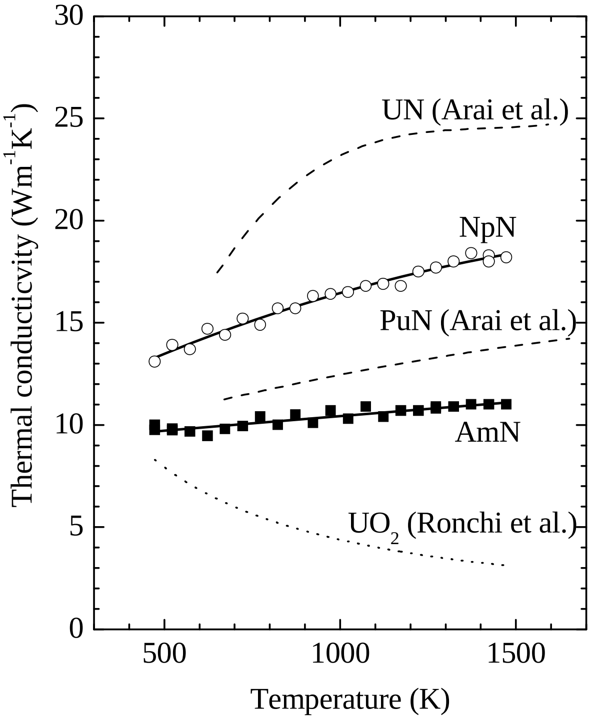

The thermal conductivity of NpN obtained was in good agreement with the reported values in the temperature range 740 to 1 173 K [6]. It was found that the thermal conductivities of NpN and AmN gradually increased with temperature over the temperature range investigated, which was the same tendency as UN and PuN. According to the literature [21,22], the thermal conductivities of UN and PuN slightly increased with temperature due to the electronic component. It can be presumed that the increase in the thermal conductivities of NpN and AmN is probably due to the electronic component. It was also found that the thermal conductivities of actinide nitrides were decreased with increasing atomic number from U to Am. Actually, the electrical conductivities of UN, NpN and PuN have a tendency to decrease with increasing atomic number from U to Pu [7]. Thus, it was consistent that the thermal conductivity of AmN was smaller than those of UN, NpN and PuN. It was also found that the thermal conductivities of NpN and AmN were still larger than that of UO_2 in the temperature range 473 to 1 473 K. The results reflect the theory that the main thermal transport mechanism of UO_2 is likely explained by phonon, whereas those of actinide nitrides are quite likely to be controlled by the electron transport.

Conclusions

The thermal diffusivities of NpN and AmN were successfully measured by the laser flash method. The heat capacities of NpN and AmN were determined by using the drop calorimetry. The conclusions were as follows:

- The thermal diffusivity of NpN was kept unchanged and that of AmN slightly decreased with increasing temperature from 473 to 1 473 K.
- The heat capacities of NpN and AmN were expressed by C_p ($Jmol^{-1}K^{-1}$) = 1.872×10^{-2} T + 42.75 ($334 \leq T$ (K) $\leq 1\,067$) and C_p ($Jmol^{-1}K^{-1}$) = 1.563×10^{-2} T + 42.44 ($354 \leq T$ (K) $\leq 1\,071$), respectively. The heat capacity of NpN was close to those of UN and PuN, while that of AmN was slightly smaller than those of UN, NpN and PuN.
- The thermal conductivities of NpN and AmN were estimated from the measured thermal diffusivity, bulk density and heat capacity. The thermal conductivities of NpN and AmN were expressed by $\lambda(Wm^{-1}K^{-1}) = -1.98 \times 10^{-6} T^2 + 0.00890\ T + 9.53$ and $\lambda(Wm^{-1}K^{-1}) = -2.54 \times 10^{-8} T^2 + 0.00147\ T + 8.99$ ($473 \leq T$ (K) $\leq 1\,473$), respectively. The thermal conductivities of NpN and AmN gradually increased with temperature over the temperature range investigated, which was the same tendency as UN and PuN. It can be presumed that the increase in the thermal conductivities of NpN and AmN are probably due to the electronic component.
- The thermal conductivity of AmN was smaller than those of UN, NpN and PuN, whereas that of AmN was larger than that of UO_2. The results reflect the theory that the main thermal transport mechanism of UO_2 is likely explained by phonon, whereas those of actinide nitrides are quite likely to be controlled by the electron transport.

Acknowledgements

The present study was carried out within the task “Technological Development of a Nuclear Fuel Cycle Based on Nitride Fuel and Pyrochemical Reprocessing” entrusted from the Ministry of Education, Culture, Sports, Science and Technology of Japan. The authors are grateful to Mr. M. Kamoshida, Chiyoda Maintenance Corporation for his kind support.

References

[1] Mignanelli, M., R. Thetford, *Thermophysical and Chemical Properties of Minor-Actinide Fuels, in Advanced Reactors with Innovative Fuels*, OECD/NEA, Paris (2001), p. 161.

[2] Minato, K., *et al.*, “Research on Nitride Fuel for Transmutation of Minor Actinides”, *Proc. AccApp/ADTTA’01*, Reno, Nevada, 11-15 November 2001, CD-ROM.

[3] Minato, K., *et al.*, *J. Nucl. Mater.*, 320, 18 (2003).

[4] Thetford, R., M. Mignanelli, *J. Nucl. Mater.*, 320, 44 (2003).

[5] Arai, Y., *et al.*, *J. Nucl. Mater.*, 195, 37 (1992).

[6] Arai, Y., Y. Okamoto, Y. Suzuki, *J. Nucl. Mater.*, 211, 248 (1994).

[7] Arai, Y., K. Nakajima, Y. Suzuki, *J. Alloys. Comp.*, 271-273, 602 (1998).

[8] Nishi, T., *et al.*, *J. Nucl. Mater.*, 355, 114 (2006).

[9] Oetting, F.L., J.M. Leitnaker, *J. Chem. Thermodynam.*, 10, 941 (1978).

[10] Nishi, T., *et al.*, *J. Nucl. Mater.*, 376, 78 (2008).

[11] Cezairliyan, A., T. Baba, R. Taylor, *Int. J. Thermophys.*, 15, 317 (1994).

[12] Josell, D., J. Warren, A. Cezairliyan, *J. Appl. Phys.*, 78, 6867 (1995).

[13] Nishi, T., *et al.*, JAERI-Tech 2005-051 (2005) (in Japanese).

[14] Nishi, T., *et al.*, *J. Nucl. Mater.* 377, 467 (2008).

[15] Barin, I., *Thermochemical Data of Pure Substance*, VCH, New York (1989), p. 48.

[16] Schulz, B., *High Temp.-High Press.*, 13, 649 (1981).

[17] Bakker, K., H. Kwast, E.H.P. Cordfunke, *J. Nucl. Mater.*, 223, 135 (1995).

[18] Hayes, S.L., J.K. Thomas, K.L. Peddicord, *J. Nucl. Mater.* 171, 300 (1990).

[19] Nakajima, K., Y. Arai, *J. Nucl. Sci. Technol.*, Supplement 3, 620 (2002).

[20] Ronchi, C., *et al.*, *J. Appl. Phys.*, 85, 776 (1999).

[21] Endebrook, R.W., E.L. Foster, D.L. Keller, US Report BMI-1690 (1964).

[22] Keller, D.L., US Report BMI-1809 (1967).

Molybdenum-CERMET fuel concept for rapid incineration of minor actinides in fast reactors*

M. Osaka, K. Tanaka, S. Miwa
Japan Atomic Energy Agency, Japan

K. Kurosaki, M. Uno, S. Yamanaka
Graduate School of Engineering, Osaka University, Japan

S. Takano, Y. Yamane
Graduate School of Engineering, Nagoya University, Japan

Abstract

A novel molybdenum-CERMET fuel concept is presented with its related cycle technologies in a fast reactor cycle system. The CERMET fuel consists of (Th,MA)O_{2-x} (host) combined with Mo inert matrix. Thoria and Mo were selected so as to enhance the fuel performance. In particular, chemical stability under irradiation is expected to be enhanced by a stabilising effect of thoria-addition and an oxygen buffering function of Mo. Related cycle technologies to the present CERMET fuel were designed with emphasis on adaptability to the existing/standard technologies for the fast reactor cycle considered in Japan. Attachment of a small sub-cycle was considered for the CERMET fuel, which aimed at a small impact on the main fast reactor cycle driven by a MOX fuel. Basic fabrication technique for the CERMET fuel was established by sintering with metal additives. Palladium was found to be one of the best sintering additives for the densification of Mo-CERMET. The Pd-addition formed a liquid phase, which enhanced atomic diffusion and grain re-arrangement by a typical mechanism of sintering in the presence of liquid phase. Moreover, Pd liquid phase froze at final stage of sintering to stabilise the sintered CERMET body. This was due to increase of melting temperature of Pd-based liquid phase by reactions with Mo. An evaluation for defect structures in thoria solid solution phase was carried out by a molecular dynamic simulation. (Th,Gd)O_{2-x} phases were selected as a representative host phase that contains MA/FP for the present evaluation. A partial ionic model including the co-valent contribution was used for the atomic potential function. Potential parameters were optimised by analysis of experimental lattice thermal expansion of component binary oxides, ThO_2 and c-type Gd_2O_3. Several defect structures, such as oxygen vacancy point defect and Gd-oxygen vacancy-Gd cluster, were assumed and lattice parameters as a function of Gd content and temperature were calculated. It was indicated from comparison between calculated and experimental results that the Gd-oxygen vacancy-Gd cluster was likely to form. Evolution of oxygen potential of thoria solid solution phase during burn-up was predicted by a chemical thermodynamic method. This prediction resulted in preferred U-addition to the thoria phase in terms of chemical stability. Core characteristics of a CERMET fuel-loaded fast reactor core were also investigated in order to seek appropriate loading conditions for the CERMET fuel. A heterogeneous composition of the CERMET fuel between inner and outer cores, namely different Mo-fraction, was found to lead both acceptable core characteristics degradation and preferable transmutation rate of MA. Such heterogeneous loading has advantages in terms of fuel fabrication since only mixing ratio of Mo and (Th,MA)O_2 powders have to be changed for the preparation of different types of CERMET fuels. The basic studies performed here have indicated that the present CERMET fuel and its related cycle technologies have a potential for the enhancement of rapid incineration of MA without a large impact on the main fast reactor cycle.

---

* The full paper being unavailable at the time of preparation of this CD-ROM, only the abstract is included.

Helium transport in a CERMET fuel matrix

Odd Runevall, Nils Sandberg, Janne Wallenius
Reactor Physics, Royal Institute of Technology, Sweden

Abstract

The effects of helium gas atoms produced by alpha decay in CERMET fuels with an inert matrix of molybdenum are studied with ab initio *methods. The theoretical study confirms the conclusions drawn from experimental data, demonstrating the presence of helium vacancy clusters. The transitions between different helium vacancy states are discussed as well as their impact on fuel swelling and helium gas release.*

Introduction

Composite fuels with an inert matrix such as ceramic ceramic (CERCER) fuels and ceramic metal (CERMET) fuels are among the many fuel candidates for transmutation purposes. Their main advantage is high thermal conductivity, with the drawback of low fissionable material density, since the inert matrix has to constitute at least 50% of the volume to achieve the desired heat conductivity. Several materials have been suggested to act as matrix in future CERCER and CERMET fuels, and due to its high melting point and thermal conductivity molybdenum is one of the materials selected for further studies within the framework of the EUROTRANS project [1].

Transmutation fuels are designed for utilisation in a fast neutron spectrum and will contain larger amounts of minor actinides compared to other fast reactor fuels. Under such operating conditions the helium production from mainly alpha decay is substantial. The gas atoms produced in such a way can either be trapped in the molybdenum matrix causing swelling and affecting mechanical properties or be released into the pin, resulting in pin pressure built-up.

Thermal desorption spectroscopy and transmission electron microscopy studies of helium in bcc molybdenum were conducted on mainly single crystals during the 80s. These studies concluded that helium atoms were trapped in vacancy defects in the crystal and formed helium-vacancy clusters, here denoted He_nV_m with n representing the number of helium atoms and m the number of vacancies in the cluster. In experiments it has been concluded that the number of vacancies in most clusters can be assumed to be close to one, whereas the number of helium atoms in a stable cluster decrease with increasing temperatures. Once a helium atom is released from a He_nV_m cluster it diffuses interstitially through the lattice almost athermally.[2-4]

The He_nV_m clusters, with n larger than one, could causes swelling of the crystal due to pressure built up in the lattice. This swelling can be hard to address under controlled experimental conditions, but can be estimated from quantum mechanical calculations, also giving possibility to study the transport phenomena of the gas atoms in much greater detail, giving a broader understanding important for fuel performance modelling.

Similar calculations have been performed for helium in bcc iron [5]. Those calculations were carried out in a comparable manner as the one here. Their conclusions are also in agreement with the conclusions draw here, however, in opposite to the molybdenum-helium system little experimental data useful for comparison with calculations exists for the iron-helium system making it hard to interpret the results from the calculations in [5].

Calculation methods

The quantum mechanical calculations were performed within the frames of the density functional theory using the VASP-code [6]. All calculations were carried out on a super cell consisting of $4 \times 4 \times 4$ cubic unit cells, in the reciprocal space a k-point grid of $3 \times 3 \times 3$ k-points were used and the kinetic energy cut-off was fixed at 500 eV. This cell size and settings were selected after converging testing on helium containing super cells.

For reference the equilibrium lattice parameter of the bulk and bulk modulus were calculated. From the bulk one atom was removed and the cohesive energy of this vacancy state was calculated. Helium atoms were then added to the vacancy position in the lattice and the cohesive energy were calculated for each He_nV_1 cluster up to $n = 4$. To avoid relaxation into symmetrical unstable states helium atoms in clusters with $n > 1$ were carefully placed in non-symmetrical positions.

To control if calculations could confirm the athermal diffusion of interstitials assumed in experiments, the formation energy for both symmetrical interstitial states, the tetrahedral and octahedral, were calculated. From those calculations one can determine the most stable interstitial states and only have to study diffusion paths in between those states. From symmetry considerations it is obvious that the diffusion path in between the octahedral state has to pass a tetrahedral state, whereas it is possible to construct a symmetrical diffusion path in between tetrahedral states without passing through an octahedral state.

All calculations, except for the reference state, were performed by first letting all atoms relax in a fixed volume and then performing a volume relaxation of the super cell. This two-step procedure was necessary to reduce the degrees of freedom, ensuring a fast enough convergence. In the case of the bulk all calculations were static and the bulk modules and lattice parameter were determined by fitting a Birch–Murnaghan potential [7] to the cohesive energy curve. From the results of the calculations, formation energies were calculated for each configuration from Eq. (1):

$$\Delta E_f(He_nV_1) = E(He_nV_1) - (127/128)\cdot E(Mo) - n\cdot E(He) \tag{1}$$

In Eq. (1) ΔE_f is the formation energy of a given configuration and E is the total energy as calculated by the code. E(He) is the energy of a free helium atom, calculated to be 0.0131 eV and E(Mo) is the cohesive energy of the reference state. As experiments have concluded the helium atoms are released one at a time from the clusters upon heating [3], this has been assumed to occur through a reaction of the form:

$$He_nV_1 \rightarrow He_{n-1}V_1 + I$$

where I represents an interstitial helium atom. Using this reaction formula, activation energies for the release of helium atoms can be calculated from the formation energies.

To assess the swelling caused by helium vacancy clusters in the lattice, the differences in the volume between helium vacancy cluster and the bulk super cells were calculated. This value corresponds to the swelling at a helium vacancy cluster to molybdenum concentration of 7 900 ppm. This concentration can be compared with the typical helium production from alpha decay in a fresh fuel of 1 800 ppm/y, this value being an upper limit for the cluster concentration since a cluster may well contain more than one helium atom.

Results

Bulk properties and a comparison with experimental values can be found in Table 1, where the experimental lattice parameter has here been extrapolated down to 0 K to give a reasonable reference to the calculations. When results from the calculations of the two interstitial states were compared, the tetrahedral state was found to be the most stable state as seen in Table 2. The calculations of the migration path in between tetrahedral states gave a migration energy of 0.053 eV, indicating that helium can find a more stable interstitial diffusion path in between tetrahedral states than the one passing through an octahedral state.

Table 1: Calculated bulk properties

	Calculations	Experiment
Lattice parameter	3.15 Å	3.14 Å
Bulk modulus	267 GPa	230 GPa

In Table 2 the calculated formation energies of the interstitial and vacancy states are presented together with activation energies for the helium release reactions. The calculated energy values tend to be slightly lower than the experimental values. This can to some extent be the attributed to the fact that no surface energy corrections are taken into account in the code. For the helium clusters, relaxation volumes were also calculated, the relative relaxation volume change is depicted in Figure 1 for the He_nV_m clusters.

Table 2: Calculated formation and activation energies

	Calculated energy	Experimental values [2,4,7]
Octrahedral site	5.45 eV	
Tetrahedral site	5.28 eV	
Vacancy state	2.69 eV	3.0-3.2 eV
$He_1V_1 \rightarrow V + I$	3.71 eV	3.8 eV
$He_2V_1 \rightarrow He_1V_1 + I$	2.67 eV	2.8-2.9 eV
$He_3V_1 \rightarrow He_2V_1 + I$	2.54 eV	2.6 eV
$He_4V_1 \rightarrow He_3V_1 + I$	2.54 eV	2.4-2.7 eV

Figure 1: Relative relaxation volumes

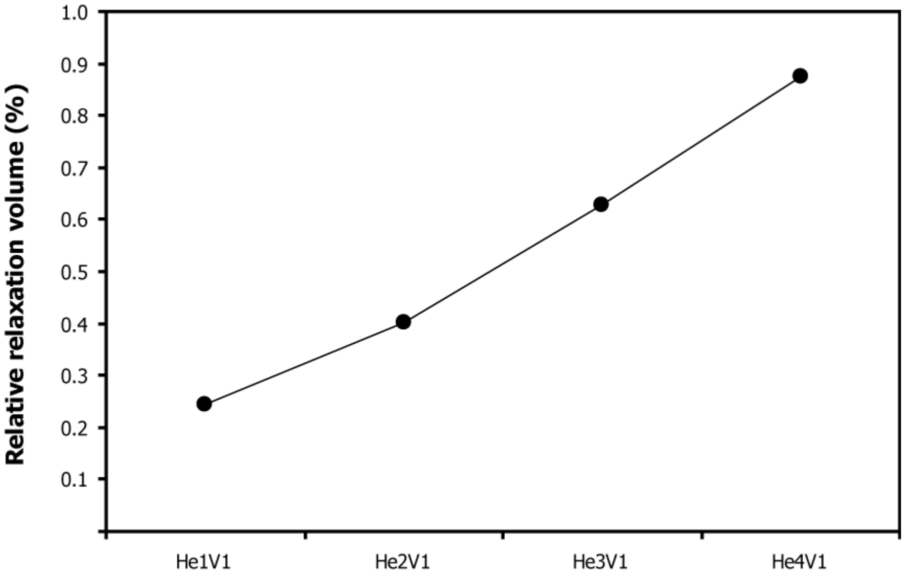

Conclusions

A typical fresh inert matrix transmutation fuel containing 7 at.% Pu, 18 at.% Am and 4 at.% Cm will have a helium production of 1 800 ppm/y and be kept at a temperature close to room temperature. This leads to helium built up in the fuel already before irradiation, and since the helium vacancy clusters are stable at room temperature one can expect a build-up of helium in the molybdenum matrix before irradiation. This will cause a small swelling prior to use which has to be accounted for when designing the fuel pin.

As temperature rises during irradiation the helium will become more mobile in the matrix and therefore diffuse out into the pin. This causes a sudden pressure build-up that should be taken into account when the cladding is designed. The DFT calculations confirm the measured activation energies for the helium release. They also confirm the experimental assumption that helium atoms in interstitial positions have a very low diffusion barrier causing almost immediate release of those atoms during a temperature increase. However, to be able to fully model this release during other conditions than a steady temperature increase more data is needed. Firstly, transition frequencies have to be calculated for these reactions and compared with experiments and secondly, other possible diffusion paths for helium have to be studied for the sake completeness.

References

[1] Maschek, W., *et al.*, “Accelerator Driven Systems for Transmutation: Fuel Development, Design and Safety”, *Progress in Nuclear Energy*, 50, 333 (2008).

[2] Van Veen, A., J.H. Evans, W.Th.M. Buters, “Percipitation in Low Energy Helium Irradiated Molybdenum”, *Radiation Effects*, 78, 53 (1983).

[3] Evans, J.H., A. Van Veen, L.M. Caspers, “The Application of TEM to the Study of Helium Cluster Nucleation and Growth in Molybdenum at 300 K”, *Radiation Effects*, 78, 105 (1983).

[4] Moore, W.T., E.V. Kornelsen, “Activation Energy and Frequency Factors for the Thermal Desorption of He Bound in Vacancies in Mo”, *Radiation Effects*, 90, 141 (1985).

[5] Fu, C., F. Willaime, “*Ab Initio* Study of Helium in bcc-Fe: Dissolution, Migration, and Clustering with Vacancies”, *Physical Review*, B, 72, 064117 (2005).

[6] Kresse, G., J. Furthmüller, “Efficient Iterative Schemes for *Ab Initio* Total-energy Calculations Using a Plane-wave Basis Set”, *Physical Review,* B, 54, 11169 (1996).

[7] Birch, F., “Finite Elastic Strain of Cubic Crystals”, *Physical Review*, 71, 809 (1947).

[8] Ehrhart, P., *et al.*, in *Atomic Defects in Metal*, Landolt-Börnstein, New Series, Group III, Vol. 25, Springer-Verlag, Berlin (1991).

Characteristics of iodides for target fabrication

Yoshiaki Tachi, Takako Donomae
Japan Atomic Energy Agency
Japan

Abstract

Some characteristics of iodides have been investigated in order to fabricate targets of long-lived radioactive iodine for transmutation by fast breeder reactors (FBR). Three kinds of fundamental experiments were performed for up to six iodides, MgI_2*,* NiI_2*, CuI, RbI,* YI_3 *and* BaI_2*, to select the most promising compound for the targets. They were: i) thermal experiments of heat iodide powders; ii) prediction experiments for compatibilities with stainless steels; iii) measurement experiments of thermal conductivities of sintered iodides. It was clarified that* BaI_2 *was the most suitable iodine compound for the FBR transmutation target and that control of impurities was very important.*

Introduction

Several long-lived fission products (LLFP) having long half-lives of more than 10 000 years are included in spent fuel waste. Transmutation of LLFP by using neutrons is very attractive technology from the viewpoint of reducing the environmental burden of spent fuel waste. Research and development concerning LLFP transmutation has been conducted in several European countries, Japan and USA. In the USA, irradiation of NaI was carried out in the Fast Flux Test Facility (FFTF) and its transmutation efficiency was estimated [1]. In Europe, a collaboration designated "Experimental Feasibility of Targets for Transmutation" (EFTTRA) was carried out which included irradiation testing of NaI, CeI_3 and PbI_2 and clarified their irradiation properties [2,3]. In Japan, fundamental research on LLFP transmutation using the accelerator-driven reactor (ADS) or fast breeder reactor (FBR) has been studied [4-6]. Tokyo Electric Power Company conducted irradiation and post-irradiation experiments with NaI, CuI and MgI_2 at the High Flux Reactor (HFR) in Petten, in collaboration with NRG [7]. Some valuable experimental data and information have been accumulated by these activities, but, much more work is needed to realise the LLFP transmutation technology. Therefore, we are conducting research and development work on the loading methods of radioactive iodine (^{129}I) into an FBR core as a part of an FBR system. ^{129}I is most important for removing a radiation exposure risk in long-term storage and it has many technical problems for loading into FBR.

Among all the LLFP nuclides in HLW, ^{99}Tc and ^{129}I have a large effect on transmutation with respect to reducing the environmental burden. Though strontium and caesium are attractive nuclides to transmute, they present large difficulties for transmutation in FBR. Strontium cannot be transmuted by the neutrons found in FBR and caesium transmutation needs isotope separation. Therefore, in our research, ^{129}I was selected as the main object for investigation of a suitable target form under FBR core conditions.

Some fundamental experiments have been conducted to clarify the most suitable form of ^{129}I under FBR core conditions, which means at elevated temperature above 773 K and under a heavy neutron irradiation for a long time, among others. In this paper, the results of those experiments and our conclusion on a suitable loading form of ^{129}I for the FBR core are described.

Selection of candidate compounds

Melting and boiling points of ^{129}I are lower than FBR core temperature. Its vapour pressure is very high around its melting point. Then, ^{129}I cannot be loaded into a FBR core in its elemental form. Thus, candidate chemical forms for loading among all binary iodides were searched for by screening applicability to FBR core conditions, fabricating and recycling conditions (reprocessing conditions). Screening like this had been done in previous studies and our search was carried out based on literature data and those previous research results. Some ternary iodides used in the previous experiments were checked as well.

For selection of the suitable iodide chemical form under FBR core conditions, a number of items were investigated for all binary iodides and some ternary iodides: *i)* characteristics of constituent elements in combination with iodine; *ii)* nuclear properties; *iii)* melting point of compounds; *iv)* compatibility with cladding materials; *v)* fabrication properties; *vi)* recycling (reprocessing) properties. Those compounds which satisfied all items were chosen as the suitable compounds.

Through the investigation of characteristics of constituent elements in combination with iodine, 29 kinds of elements and 32 compounds were chosen after excluding some elements with a lower boiling point lower than core temperature and excluding chemically active elements like halogens from all binary iodides and some ternary iodides. Next, six compounds were excluded to avoid generation of new long-lived nuclides by neutron irradiation, and six other compounds were cut because their melting points were below 873 K. Then, 14 compounds were excluded from the remaining compounds because they were not compatible with cladding materials, they easily release gases or they included impurities introduced during their fabrication or long storage before their reprocessing. As a result of these screenings, seven compounds remained, which were MgI_2, KI, NiI_2, CuI, RbI, YI_3 and BaI_2.

Experimental procedure

In order to evaluate detailed characteristics of the seven selected iodides with respect to the FBR core conditions, three fundamental out-of-pile experiments using stable ^{127}I were conducted: *i)* thermal experiments to heat iodides powders; *ii)* prediction experiments for compatibilities with cladding materials; *iii)* measurement experiments of thermal conductivities of sintered iodides. These experimental procedures are described below.

Thermal experiments of iodide powders

To understand the iodide powder behaviours at elevated temperature, powder sample of each of the chosen iodides were heated at temperatures from 60% to 80% of the respective melting point for six hours in the special test container shown in Figure 1. Iodide powder was put into the container which had an elastic function because of a bellows mechanism. This test container was set in a universal testing machine and heated to the desired temperature. If the iodide powder in the container was sintered, the bellows mechanism would shrink, and if it swelled, the bellows would expand. The quantity of shrinkage and extension of the bellows was recorded by a strain gage. During the heating experiments, the load to the iodide powder was kept at 5 MPa continuously. Conditions for the thermal experiments are shown in Table 1. Six of the iodide powders were commercially available, and they had high purity. As KI powder was not sold in Japan, the thermal experiment with KI powder was not carried out. After the thermal experiments, the test containers were opened, and the samples were removed. Outer appearances and cross-sectional microstructures were noted, X-ray diffraction measurements were made. Iodides powders were handled in a glove box filled with high-purity argon gas because the iodides are easily degraded by moisture.

Figure 1: The special test container

Table 1: Conditions of thermal experiments and purity of iodide powders

	Heating temperature [melting point] (K)	Pressuring (MPa)	Heating duration (h)	Purities of powder (%)
MgI_2	723 [923]	5	6	99.5
NiI_2	673 [1 070]			99.9
CuI	673 [878]			99.999
RbI	723 [929]			99.9
YI_3	923 [1 270]			99.9
BaI_2	773 [1 013]			99.5

Prediction experiments of compatibilities of iodides with cladding materials

To select the most suitable chemical forms for loading into a FBR core from the chosen iodides, their compatibilities with cladding materials were evaluated experimentally. Iodide powder or a sintered pellet was put into a test capsule with stainless steels. Three stainless steels, 316-stainless steel (SUS316) which would give general information on iodide compatibilities with austenitic stainless steel, ODS (oxide dispersion strengthened stainless steel) which is the most promising material for FBR cladding tubes and PNC-FMS steel (11Cr-0.5Mo-2W-V, Nb) which would give general information on iodide compatibilities with ferritic/martensitic stainless steel were estimated. A weighed disc specimen for each steel type was put in a test capsule along with the iodide powder or sintered pellet and the capsule was filled with argon gas.

These capsules were heated at 873 K for a maximum of 3 000 h in an electric furnace. After heating, capsules were opened and the disc specimens were retrieved. The retrieved specimens were evaluated regarding their compatibilities with iodides though the observation of their appearances, measurement of their mass change by an electric balance and analysis of composition change near the surface by SEM and SEM-EDX.

Measurement experiments of thermal conductivities of sintered iodides

To estimate thermal properties of iodides, their thermal diffusivities were measured by the laser flash method from room temperature to 873 K. Thermal conductivities were calculated using their densities and heat capacities stored in the material database "MALT 2". Because one of the iodides decomposed above 623 K, measurements of thermal diffusivities of all specimens above 573 K were conducted under an inert gas atmosphere. Test samples of iodide for thermal diffusivity measurements were 6 mm in diameter and 1.0 or 1.5 mm thick. Potassium iodide (KI) was a single crystal, RbI was both single crystal and poly-crystal (sintered specimen), and others were sintered discs.

Experimental results

Behaviours of heated iodide powders

Powders of CuI and BaI_2 were dense just after heating, and indicated no change of inner pressure of test container (Figure 2). The heated CuI and BaI_2 powders were shaped into pellets as seen in Figure 3. Their metallurgical microstructures were dense. They are thought to have good properties at high temperature and good properties for sintering. According to the X-ray diffraction patterns, CuI and BaI_2 included a little moisture, and it was thought to be on their surfaces. On the other hand, powders of MgI_2, RbI and YI_3 were not as dense as CuI or BaI_2 powder. Their appearances seemed to be in the middle of sintering. From the results of their X-ray diffraction patterns, they had moisture like CuI and BaI_2. The sample of NiI_2 indicated large expansion during heating, and heating was stopped before the desired temperature was reached. NiI_2 appeared to decompose at a relatively lower temperature.

Figure 2: Powder behaviours of CuI and BaI_2 during thermal experiments

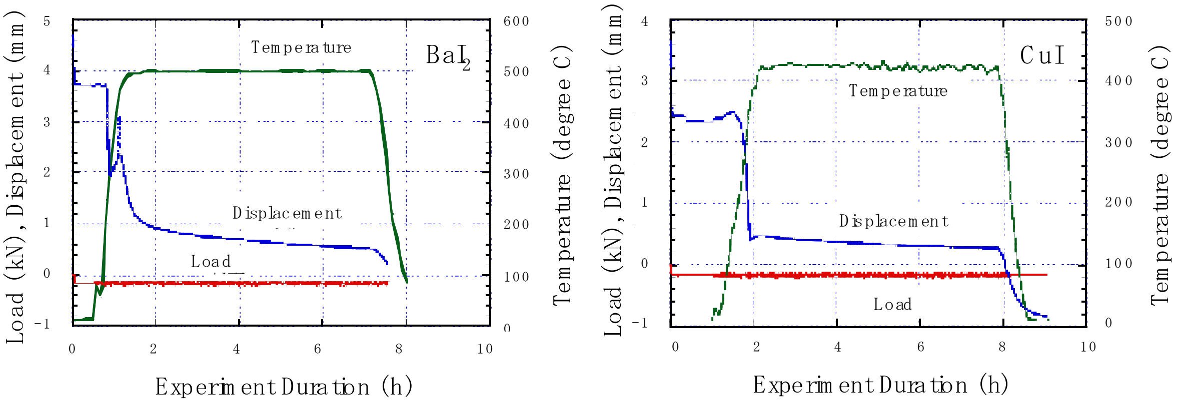

Figure 3: Appearances of CuI (left) and BaI$_2$ (right) after thermal experiments

Compatibility of iodides with cladding materials

Mass changes of test pieces of cladding materials are shown in Figure 4. Except for the experiments with CuI, mass changes of SUS316 were smaller than for the other steels. PNC-FMS indicated mass loss after the compatibility experiments, except for BaI$_2$ for 1 000 h. Mass changes of ODS showed several behaviours depending on constituent iodides. From the viewpoint of iodides, MgI$_2$, CuI, YI$_3$ and BaI$_2$ had large mass changes, more than 0.01 g/cm^2, in every cladding material, and RbI had only small mass changes for every kind of steel.

Figure 4: Mass changes of cladding materials

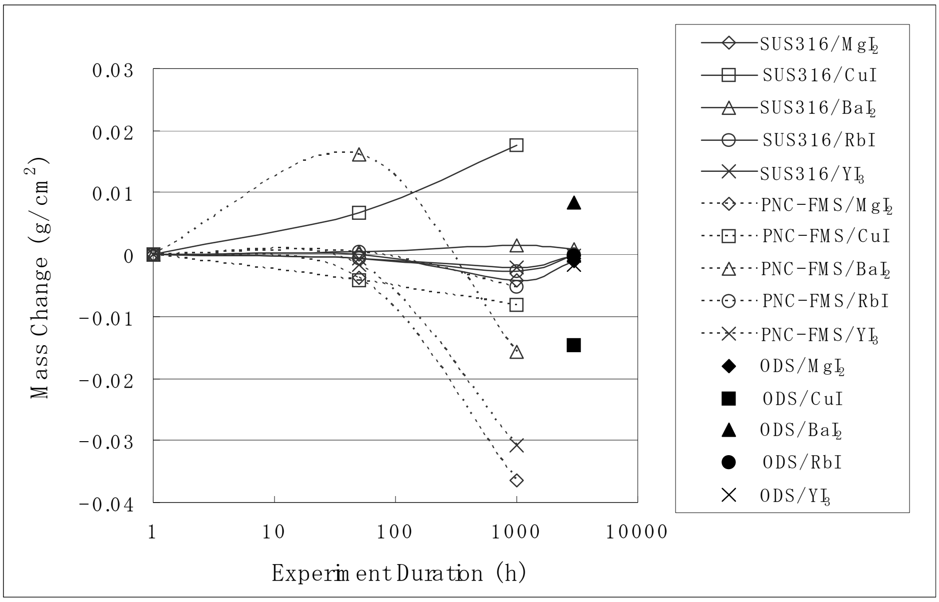

From the observations of appearances and microstructures in the cross-section of every cladding material, pit corrosions and traces of a chemical reaction were found in SUS316 in contact with MgI$_2$, CuI and YI$_3$ for 3 000 h. For the cladding materials in contact with BaI$_2$ powder for 3 000 h, oxidation layers were observed on their surfaces. In experiments with PNC-FMS for 1 000 h, except for RbI, surface degradations such as pit corrosion were observed. In ODS in contact with MgI$_2$, CuI and YI$_3$, pit corrosions occurred the same as in the SUS316 experiments. For ODS in contact with BaI$_2$, an oxidation degraded layer was observed at the surface. Oxidation layers of SUS316 and ODS are shown in Figure 5. SUS316, PNC-FMS and ODS in contact with RbI for the maximum 3 000 h did not show any remarkable changes on their surfaces according to SEM observations.

Figure5: Oxidation layer of SUS316 (left) and ODS (right) contact with BaI_2 for 3 000 h

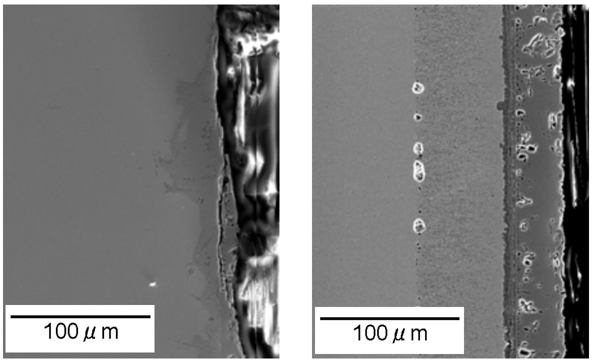

In addition, from the metallurgical observation results of the test capsules, it was clarified that there were differences on the inner surface between contact with solid iodides and contact with gaseous iodides or iodine. The lower part of the test capsule in contact with solid iodides appeared as similar to the disc specimens for all experiments, but the upper part which was in contact with gaseous iodides displayed traces of intense corrosion shown in Figure 6.

Figure 6: Surfaces of the lower part (left) and the upper part (right) of the test capsules of RbI

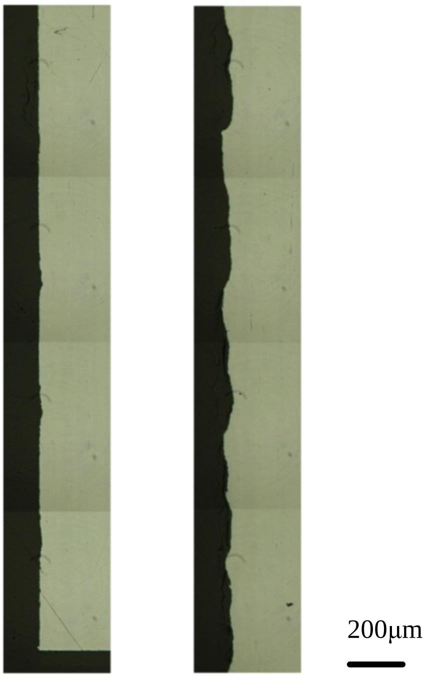

Thermal conductivities of iodides

Thermal conductivities of four kinds of iodides, CuI, KI, RbI and BaI_2, from room temperature to 873 K are shown in Figure 7. Thermal conductivities near room temperature (278-303 K) differed by the kinds of iodides and their crystal structures, *i.e.* single crystal or poly-crystal. On the other hand, above 573 K, thermal conductivities of every iodide were very small and below 0.5 W/mK. Furthermore, the temperature dependence of thermal conductivities of CuI had discontinuity between 623 K and 673 K.

Figure 7: Thermal conductivities of iodides

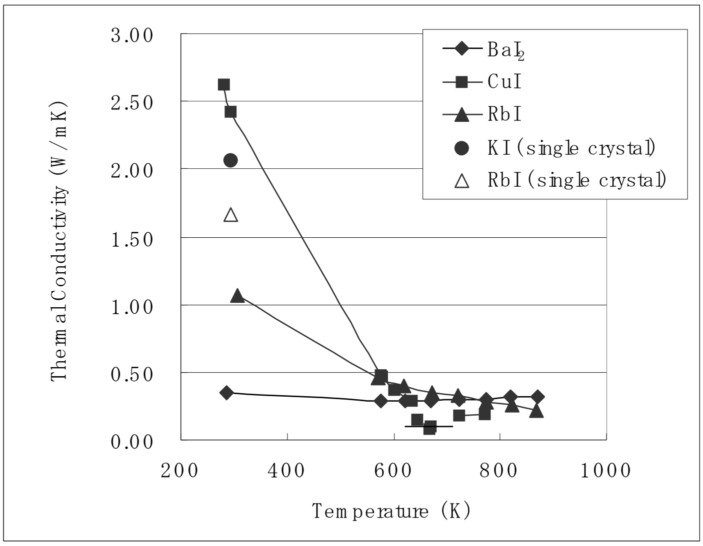

Discussion

Except for NiI_2 which expanded during heating, the chosen iodide powders were sintered to pellets with more than 80% density without decomposition. These iodides are appropriate for elevated temperature environments. The good behaviours of the iodide powders are based on their ionic bonding, and these iodides can easily be sintered to pellets by pressing. The behaviour of NiI_2 is considered to be due to its decomposing. In the test container with the elastic function, NiI_2 would be decomposed at around 603 K as reported by [8]. From the results of X-ray diffraction patterns and thermal analysis, increasing the inner pressure of BaI_2 powder by heating is attributed to crystalline H_2O. The crystalline H_2O with BaI_2 was introduced during powder fabrication but it should be removed when powder is prepared as a target.

As for compatibilities of iodides with cladding materials, chemical interactions between iodides and cladding materials were studied thermodynamically. According to their free energies shown in Figure 8, interactions between cladding materials and MgI_2 or YI_3 are guessed not to be caused. In the interaction between cladding materials and CuI, reactions of Cr and Mn with iodine can progress thermodynamically. From these thermodynamic studies, it seems that pit corrosion of cladding materials by MgI_2 or YI_3 depended on the influence of impurities, O_2 and/or H_2O in the atmosphere contained in the test capsule. These impurities and iodides are considered to destroy the passivity of cladding materials. Oxidation layers of cladding materials in contact with BaI_2 are considered to be generated by impurities of O_2 and/or H_2O in BaI_2 powder. The reason that the oxidation layer was not observed in PNC-FMS in contact with BaI_2 for 1 000 h is attributed to use of sintered BaI_2. The crystalline H_2O in BaI_2 was removed during sintering. Therefore, it is very important to control impurities, especially crystalline H_2O, to get good compatibilities between cladding materials and iodides. In the compatibility experiments for 1 000 h, differences of mass change behaviours between SUS316 and PNC-FMS are considered to depend on their crystal structures. The penetration of O atoms in the BCC structure of PNC-FMS is thought to be easier than in the FCC structure of SUS316, likely as shown to the form of oxidation layers in both steels by BaI_2. And, severe degradation of the inner surface of the test capsule (SUS316) in contact with gases is thought to be caused by gaseous iodide compounds and/or their constituents [9].

On the other hand, thermal conductivities of iodides are very small like most non-metallic materials, because their heat transfer is dominated by phone conduction and it is disturbed by increasing temperature. Changes of thermal conductivities of CuI from 623 K to 673 K are predicted to be caused by the phase transfers of CuI, *i.e.* alpha-phase of CuI transfers to the beta-phase at 629 K and beta-phase transfers to the gamma-phase at 680 K.

Figure 8: Free energy of reaction between iodides and constituents of cladding materials

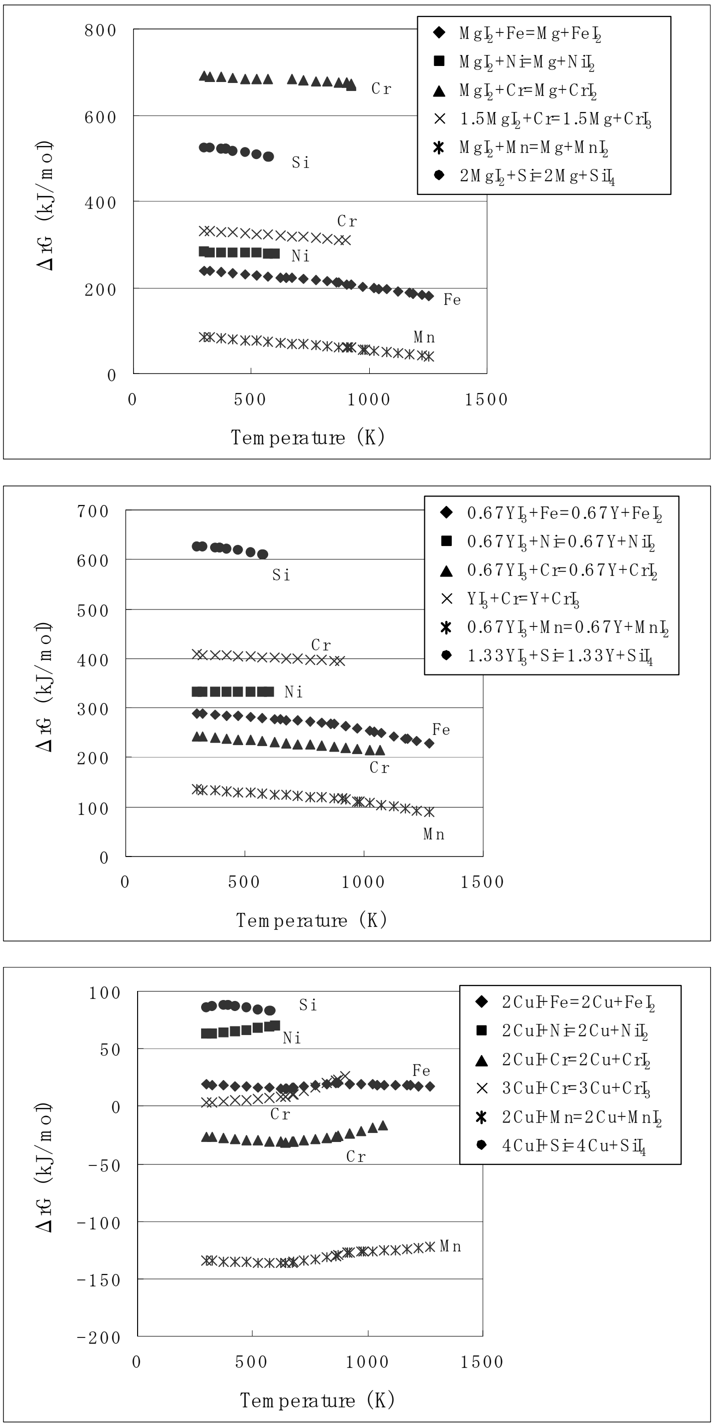

Conclusion

The most important point for loading iodides into a FBR core is that iodides have good compatibility with cladding materials and they do not decompose during transmutation. Through the experiments and studies concerning the characteristics of iodides, it was determined that NiI_2 is not appropriate because of its decomposition, and MgI_2, CuI and YI_3 are not, either, because of their incompatibility with cladding materials. On the other hand, RbI showed good compatibility with cladding materials when the contact was with solid RbI, but when the contact was with gaseous RbI severe degradation occurred, so it was thought to be unsuitable for loading in the FBR core. According to all the results, BaI_2 was considered to be the most suitable chemical form for a transmutation by a FBR, however, it is very important to control the impurities in BaI_2 during its fabrication so as to avoid cladding tube degradation.

Acknowledgements

Dr. M. Hirai at NFD is acknowledged for technical support of the experiments. Dr. N. Akasaka at JAEA is thanked for critical reading of the manuscript.

References

[1] Wootan, D.W., D.P. Jordheim, W.Y. Matsumoto, *Trans. Am. Nucl. Soc.*, 64, 125 (1991).

[2] Konings, R.J.M., *J. Nucl. Mater.*, 244, 16-21 (1997).

[3] Konings, R.J.M., *et al.*, *Nucl. Tech.*, 117, 293-298 (1997).

[4] Nishihara, K., H. Takano, *Nucl. Tech.*, 137, 47 (2002).

[5] Shirasu, Y., K. Minato, *J. Nucl. Mat.*, 320, 25-30 (2003).

[6] Takaki, N., T. Mizuno, *Proceedings of International Conference on Global Environment and Advanced Nuclear Power Plants (GENES4/ANP2003)*.

[7] Ichimura, E., *et al.*, *J. Nucl. Mater.*, 334, 149-158 (2004).

[8] *Binary Alloy Phase Diagrams*, 2nd Edition.

[9] Wren, J.C., G.A. Glowa, J. Merritt, *J. Nucl. Mater*. 265, 161-177 (1999).

Thermal expansion of TRU nitrides as the fuel materials for transmutation of minor actinides

Masahide Takano, Mitsuo Akabori, Yasuo Arai, Kazuo Minato
Nuclear Science and Engineering Directorate
Japan Atomic Energy Agency

Abstract

As the research activities concerning the nitride fuel for the transmutation of minor actinides, the lattice thermal expansions of the transuranium nitrides were investigated in order to build the materials database. The lattice parameters of NpN, PuN and AmN were measured using the high temperature X-ray diffraction method from room temperature to 1 478 K. Their linear thermal expansions were determined as a function of temperature. The average thermal expansion coefficients over the temperature range 293-1 273 K for these nitrides were 8.8, 11.1 and 11.2 $\times 10^{-6}$ K^{-1}*, respectively. Further, the thermal expansions of the nitride solid solution samples, (Np,Am)N, (Pu,Am)N, (Np,Pu,Am,Cm)N and (Pu,Am,Zr)N, were measured to investigate the composition dependence. It was confirmed that the average thermal expansion coefficients for these solid solution samples could be approximated by the linear mixture rule within the error of 2-3%.*

Introduction

Actinide nitrides are considered as the potential fuel/target material for the transmutation of minor actinides (MA: Np, Am, Cm) in fast reactors and also in the accelerator-driven systems (ADS) [1,2]. The excellent thermal and neutronic properties of the nitride fuel may enable the high concentration of actinides. Also the flexibility in actinide composition will be expected from the mutual solubility among the actinide mononitrides [3]. In JAEA, the research activities concerning the heterogeneous MA-recycling based on the nitride fuel and pyrochemical reprocessing are going on as one of the optional strategies. The present authors have been studying on the basic thermal properties of transuranium (TRU) nitrides in order to build the materials database needed for the fuel design and for understanding the fuel behaviour.

Thermal expansion data are used to evaluate the change in dimensions and density of a fuel pellet with temperature. Dilatometry is a usual method to measure the bulk expansion direct. However, some factors like porosity, sintering, or surface oxidation affect the data. In addition, it is not easy to prepare a pellet-sized specimen of the pure Am or Cm nitride. On the other hand, the lattice thermal expansion measured by the high temperature X-ray diffraction (XRD) method is rather fundamental data to understand the bulk expansion. This method is useful especially for measurements on the TRU compounds since the precise data can be obtained with the smaller amount of sample.

As for the situation of lattice thermal expansion data on actinide mononitrides, some data sets for UN are available in literature and they were reviewed by Hayes, *et al.* [4]. However, those for the TRU nitrides are very scarce except for the low temperature data on NpN [5] and PuN [6]. Recently we have succeeded in measuring the lattice thermal expansion of NpN, PuN and AmN [7] as the main constituents of the nitride fuel for MA transmutation. Further, those of the TRU nitride solid solution samples, (Np,Am)N, (Pu,Am)N, (Np,Pu,Am,Cm)N and (Pu,Am,Zr)N, where ZrN was added as the inert matrix, have been measured to develop a correlation between the thermal expansion coefficients for the constituent nitrides and their solid solutions [8]. This paper presents the results of these systematic studies on the thermal expansion of TRU nitrides.

Experimental

Preparation of nitride samples

NpN, PuN and AmN were synthesised from the powder of $^{237}NpO_2$, PuO_2 and $^{243}AmO_2$ by the carbothermic reduction method. Details are described elsewhere [7]. To prepare the binary TRU nitride solid solution samples, the mixtures of NpN/AmN and PuN/AmN were compacted and heated at 1 830-1 870 K in N_2-4%H_2 mixed gas flow for seven hours. Two or three cycles of pulverisation, compaction and heat treatment yielded the single-phase solid solution with the sharp XRD peaks, respectively. The compositions were determined to be $(Np_{0.55}Am_{0.45})N$ and $(Pu_{0.59}Am_{0.41})N$, taking the weight loss due to the evaporation of AmN into consideration.

A part of (Pu,Am)N sample was blended with ZrN as the inert matrix. Two cycles of the similar heat treatment yielded the single-phase solid solution of $(Pu_{0.21}Am_{0.18}Zr_{0.61})N$. The powder of highly pure ZrN was synthesised from metal through hydride. The composition of the light elements after annealing at 1 770 K in N_2 gas flow for five hours was determined to be $Zr(N_{0.993}O_{0.006}C_{0.001})_{0.97}$ by the quantitative analyses on nitrogen, oxygen and carbon.

The quaternary nitride containing Np, Pu, Am and Cm was prepared from the oxide mixture of $^{237}NpO_2/PuO_2/^{243}AmO_2/(^{240}Pu,^{244}Cm)O_2$ by the simultaneous carbothermic nitridation. The product was compacted again and heated at 1 910 K for four hours for homogenisation. The composition was determined to be $(Np_{0.21}Pu_{0.52}Am_{0.22}Cm_{0.05})N$, taking the evaporation loss of Am into consideration.

High temperature X-ray diffraction method

Lattice parameters of the nitride powder samples were measured by the high temperature XRD method as a function of temperature. Goniometer installed in a glove box with a purified argon atmosphere was employed to avoid the oxidation and/or hydrolysis of the nitride samples. About

20 mg of each powder sample was loaded on a platinum or tungsten holder. The XRD profiles were recorded with Mo-Kα radiation from room temperature to 1 478 K, at every 100 K. The sample temperature was monitored by a thermocouple inserted into the holder. The atmosphere of the sample chamber was kept with N_2-4%H_2 mixed gas flow during the high temperature measurements. To reduce the effect of self-irradiation damage on the lattice parameter, especially for the sample containing ^{244}Cm, the XRD measurement was started immediately after the heat treatment. The lattice parameters calculated from 8-10 diffraction peaks were refined using the Nelson-Riley function. The uncertainty in the lattice parameter determination was within ±0.00004 nm.

Results and discussion

Some examples of the XRD profiles at room temperature are shown in Figure 1 (left). Each product was identified as the single-phase nitride with NaCl-type structure. Any oxide phases other than the sample holder were not recognised. Split of the $K\alpha_1$ and $K\alpha_2$ peaks was enough to determine the $K\alpha_1$ peak positions precisely.

Figure 1: Partial XRD profiles of the nitride samples (left), and lattice parameters at room temperature as a function of composition (right)

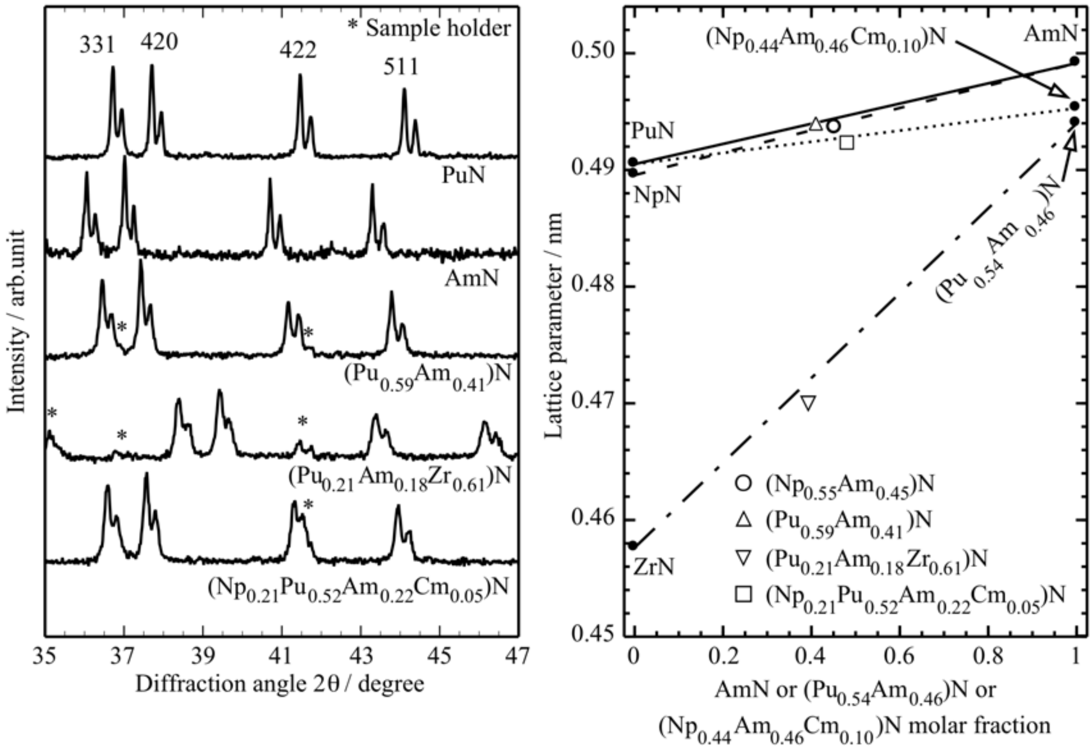

The lattice parameters of NpN, PuN and AmN at room temperature were 0.48960, 0.49053 and 0.49915 nm, respectively. That of NpN prepared by Suzuki, *et al.* [9] is 0.48968 nm with the oxygen and carbon contents of 0.03 and 0.09 wt.%. Muromura [10] estimated that of "pure" PuN to be 0.49049 nm from the data on PuN samples with the various oxygen and carbon contents. Another AmN sample prepared by the present authors with 0.05 wt.% oxygen and 0.02 wt.% carbon had 0.49911 nm. Comparing with these values, the oxygen and carbon contents in the prepared NpN, PuN and AmN samples were considered to be fairly low.

The lattice parameters of the solid solution samples at room temperature are plotted in Figure 1 (right) against the molar fraction of AmN, $(Np_{0.44}Am_{0.46}Cm_{0.10})N$ or $(Pu_{0.54}Am_{0.46})N$, where the compositions of $(Np_{0.21}Pu_{0.52}Am_{0.22}Cm_{0.05})N$ and $(Pu_{0.21}Am_{0.18}Zr_{0.61})N$ are expressed as 0.52PuN-0.48$(Np_{0.44}Am_{0.46}Cm_{0.10})N$ and 0.61ZrN-0.39$(Pu_{0.54}Am_{0.46})N$, respectively. The lines represent the Vegard's law between NpN-AmN, PuN-AmN, PuN-$(Np_{0.44}Am_{0.46}Cm_{0.10})N$ and ZrN-$(Pu_{0.54}Am_{0.46})N$, respectively. The data for $(Pu_{0.54}Am_{0.46})N$ and $(Np_{0.44}Am_{0.46}Cm_{0.10})N$ were calculated by the Vegard's law using our data and the literature value of 0.5027 nm for CmN [11]. The measured lattice parameters of the binary and quaternary TRU nitrides agreed reasonably with those calculated by the Vegard's law. However, the $(Pu_{0.21}Am_{0.18}Zr_{0.61})N$ sample showed a slightly smaller value than the calculated one as is seen in Figure 1 (right).

The lattice parameters of the nitride samples are shown in Figure 2 as a function of temperature. The solid curves represent the least square fitting to a third-order polynomial. The regression results were shown in the earlier papers [7,8]. The maximum deviation from the fitted curve was 0.00008 nm for the $(Pu_{0.59}Am_{0.41})N$ sample at 1 375 K, and within 0.00004 nm for the other data points. The symbol "x" in the figure corresponds to the results after the high temperature measurements. The excellent reproducibility at room temperature was confirmed for each sample, namely the difference was within 0.00003 nm. This means that the change in the dissolved oxygen content or in the actinide composition during the high temperature measurements was negligible.

Figure 2: Lattice parameters of the nitride samples as a function of temperature

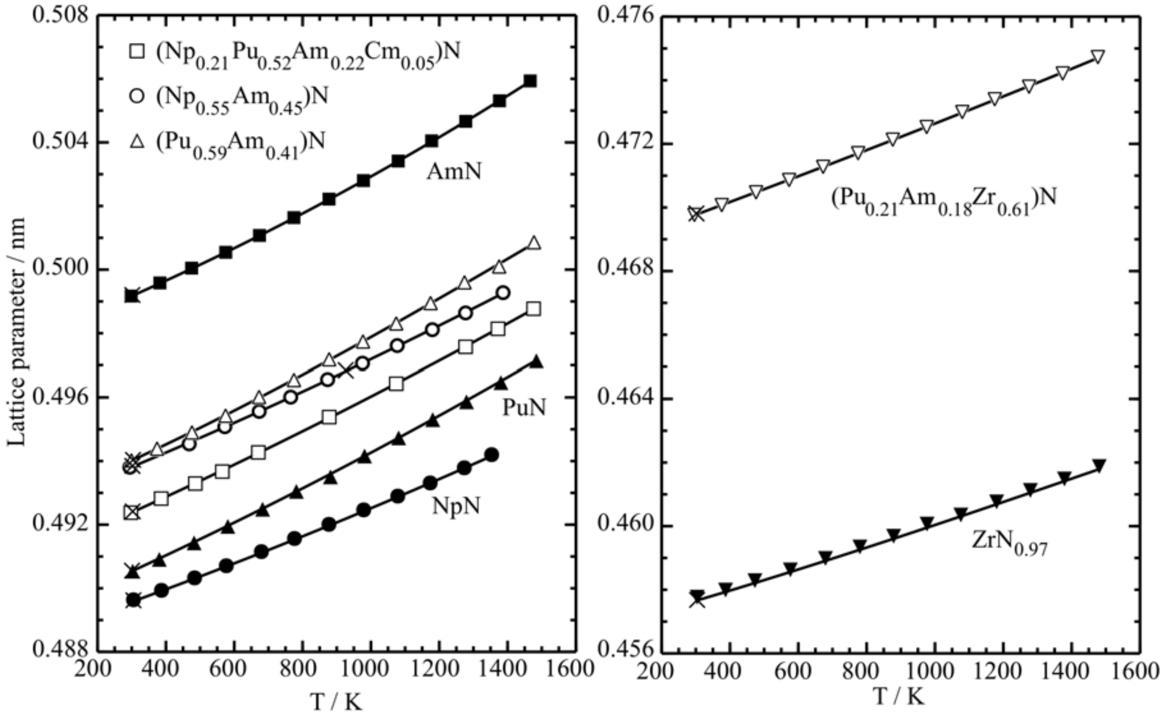

The linear thermal expansion, LTE (%), from the reference temperature 293 K for each nitride sample was calculated by the definition:

$$\text{LTE (\%)} = 100\,(a_T - a_{293})/a_{293} \tag{1}$$

where a_T and a_{293} are the lattice parameters at temperature T and 293 K. Figure 3 shows the linear thermal expansions for the single-component nitride samples (left) and the solid solution samples (right) with the reviewed data on UN [4]. The solid and dotted curves represent the least square fitting to the following equation:

$$\text{LTE (\%)} = b_1\,(T\text{-}293) + b_2\,(T\text{-}293)^2 + b_3\,(T\text{-}293)^3 \tag{2}$$

where b_1, b_2 and b_3 are the fitting constants. Fitting results are listed in Table 1, together with the a_{293} values, the LTE values at 1 273 K, and the average thermal expansion coefficients, α, over the temperature range of 293 to 1 273 K. The maximum error of 2% for the α_{1273} values was estimated from the uncertainty in the lattice parameter determination.

Among the single-component TRU nitrides, PuN and AmN were found to have the large LTE_{1273} values (1.09-1.10%) compared with those for NpN and UN (0.86-0.87%). The LTE_{1273} values for the binary and quaternary TRU nitride solid solution samples ranged from 0.99% for $(\mathrm{Np}_{0.55}\mathrm{Am}_{0.45})\mathrm{N}$ to 1.13% for $(\mathrm{Pu}_{0.59}\mathrm{Am}_{0.41})\mathrm{N}$. That for (Pu,Am)N diluted with ZrN was lowered to 0.86% due to the effect of the lower LTE_{1273} value of 0.74% for ZrN.

Table 1: Fitting constants for Eq. (2) together with a_{293}, LTE_{1273}, and α_{1273} values

Composition	b_1 (10^{-4})	b_2 (10^{-8})	b_3 (10^{-12})	a_{293} (nm)	LTE_{1273} (%)	α_{1273} ($10^{-6}\mathrm{K}^{-1}$)
UN [4]	7.505	14.07	0	0.48892	0.87	8.88
NpN	7.827	11.42	-15.34	0.48956	0.86	8.80
PuN	9.973	12.88	-9.445	0.49050	1.09	11.1
AmN	9.387	19.28	-6.052	0.49915	1.10	11.2
$(\mathrm{Np}_{0.55}\mathrm{Am}_{0.45})\mathrm{N}$	9.139	9.866	-5.024	0.49377	0.99	10.1
$(\mathrm{Pu}_{0.59}\mathrm{Am}_{0.41})\mathrm{N}$	10.04	18.91	-41.41	0.49398	1.13	11.5
(Np,Pu,Am,Cm)N[a]	9.872	9.671	-0.8295	0.49235	1.06	10.8
$(\mathrm{Pu}_{0.21}\mathrm{Am}_{0.18}\mathrm{Zr}_{0.61})\mathrm{N}$	8.375	4.686	-2.484	0.46975	0.86	8.82
$\mathrm{ZrN}_{0.97}$	6.929	8.741	-22.00	0.45763	0.74	7.57

[a] $(\mathrm{Np}_{0.21}\mathrm{Pu}_{0.52}\mathrm{Am}_{0.22}\mathrm{Cm}_{0.05})\mathrm{N}$.

Correlation between the average thermal expansion coefficients for the solid solution samples and for the constituent nitrides is discussed as follows. Figure 4 shows the plots of α_{1273} (left) and extrapolated α_{1773} values (right) for the solid solution samples against the molar fraction of AmN, $(\mathrm{Np}_{0.44}\mathrm{Am}_{0.56})\mathrm{N}$ or $(\mathrm{Pu}_{0.54}\mathrm{Am}_{0.46})\mathrm{N}$. The dotted lines represent the hypothetical "linear mixture rule". The measured α_{1273} values for $(\mathrm{Np}_{0.55}\mathrm{Am}_{0.45})\mathrm{N}$ and $(\mathrm{Pu}_{0.59}\mathrm{Am}_{0.41})\mathrm{N}$ are 2.2 and 3.2% greater than the coefficients at corresponding AmN fractions on the NpN-AmN and PuN-AmN lines, respectively.

Figure 4: Plots of α_{1273} (left) and α_{1773} (right) in comparison with the linear mixture rule

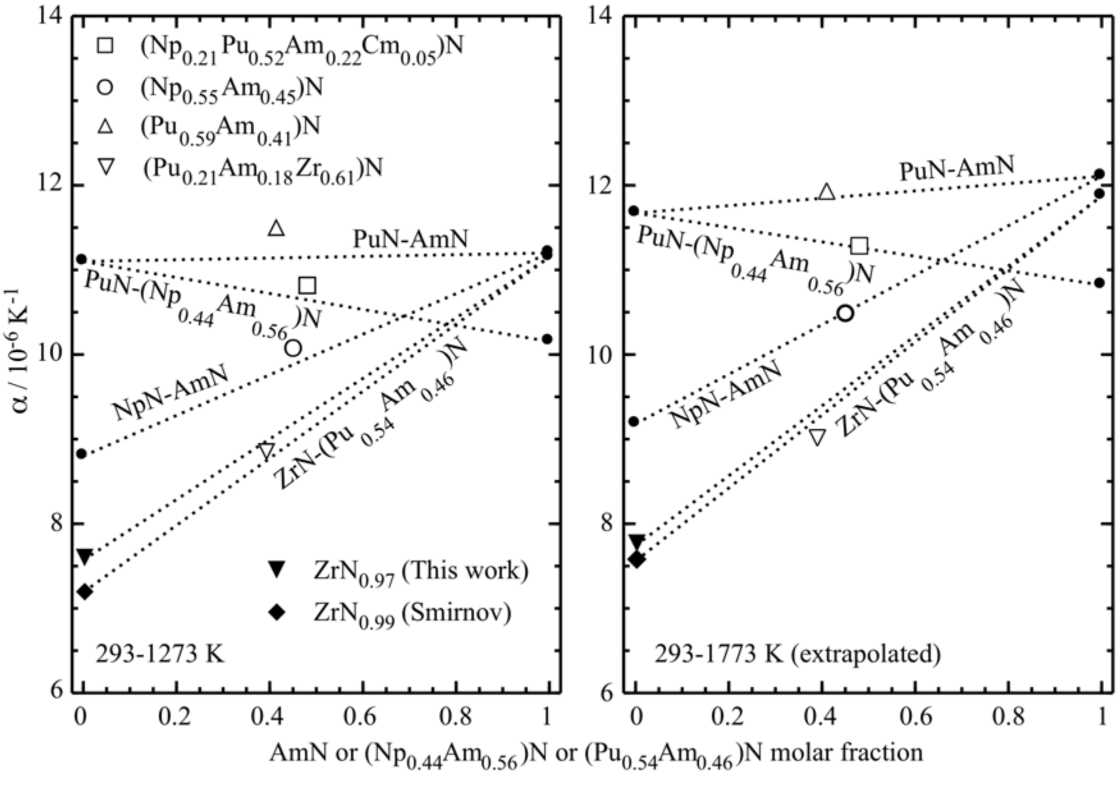

For the $(Np_{0.21}Pu_{0.52}Am_{0.22}Cm_{0.05})N$ sample, since the CmN content is relatively low and its data is still missing, the Cm fraction was included in Am for convenience. Then, the measured data was plotted as $0.52PuN\text{-}0.48(Np_{0.44}Am_{0.56})N$ in Figure 4. The measured α_{1273} value is 1.5% greater than the coefficient on the $PuN\text{-}(Np_{0.44}Am_{0.56})N$ line. If the α_{1273} value for CmN lies in interval of $10\text{-}12 \times 10^{-6}$ K^{-1}, that for $(Np_{0.21}Pu_{0.52}Am_{0.22}Cm_{0.05})N$ is calculated to be $10.6\text{-}10.7 \times 10^{-6}$ K^{-1}. In this case the measured value is 1.1-2.0% greater.

A possible reason for the slightly greater α_{1273} values than the calculated ones would be the influence of dissolved oxygen. The dissolved oxygen contents in the solid solution samples were considered to be higher to some extent than those in the NpN, PuN and AmN samples used for the thermal expansion measurements, because of the repeated heat treatment cycles to form the solid solution.

The solid solution sample of $(Pu_{0.21}Am_{0.18}Zr_{0.61})N$ can be expressed as $0.61ZrN\text{-}0.39(Pu_{0.54}Am_{0.46})N$. The measured α_{1273} value is 1.6% smaller than the coefficient on the $ZrN_{0.97}\text{-}(Pu_{0.54}Am_{0.46})N$ line, which shows the opposite tendency to the other solid solution samples. Another α_{1273} value for the near stoichiometric $Zr(N_{0.994}O_{0.002}C_{0.004})_{0.993}$ obtained by Smirnov, *et al.* [12] is $(7.19\pm0.28) \times 10^{-6}$ K^{-1}. As the oxygen and carbon contents are not so different from those in the $ZrN_{0.97}$ sample, the hypostoichiometric feature of ZrN may possibly affect the thermal expansion coefficient. A similar effect is known in case of the fluorite $(U,Pu)O_{2-x}$, where the α value increases considerably with increasing x value [13]. When using the α_{1273} value for $ZrN_{0.99}$, the measured value is 1.0% greater than the coefficient on the $ZrN_{0.99}\text{-}(Pu_{0.54}Am_{0.46})N$ line. The (N+O+C)/(Pu+Am+Zr) ratio of the $(Pu_{0.21}Am_{0.18}Zr_{0.61})N$ sample was then presumed to be around 0.98-0.99, though the chemical analysis was not performed.

In addition to the comparison at 1 273 K, the excellent agreement between the measured and calculated α values extrapolated to 1 773 K was also confirmed as is seen in Figure 4 (right). The deviations tend to become somewhat greater at the lower temperatures except for the nitride diluted with ZrN.

From the above discussion, it was confirmed that the average thermal expansion coefficients for the TRU nitride solid solutions could be estimated by the linear mixture rule within the error of 2-3%, even in the case for the nitride diluted with ZrN. In order to make more precise estimations, the influence of dissolved oxygen content and the hypostoichiometry of the ZrN-containing nitride should be investigated quantitatively, as well as the thermal expansion data on CmN.

Conclusions

Lattice parameters of NpN, PuN, AmN and the nitride solid solution samples, $(Np_{0.55}Am_{0.45})N$, $(Pu_{0.59}Am_{0.41})N$, $(Np_{0.21}Pu_{0.52}Am_{0.22}Cm_{0.05})N$ and $(Pu_{0.21}Am_{0.18}Zr_{0.61})N$, were measured by the high temperature XRD method from room temperature to 1 478 K. Their linear thermal expansions from 293 K were determined as a function of temperature. The average thermal expansion coefficients for the solid solution samples were compared systematically with those for the constituent nitrides. It was confirmed that the linear mixture rule could be applicable to estimate the thermal expansion coefficients for the solid solution samples within the error of 2-3%.

Acknowledgements

The present study includes the result of “Technological Development of a Fuel Cycle Based on Nitride Fuel and Pyrochemical Reprocessing” entrusted to the Japan Atomic Energy Agency by the Ministry of Education, Culture, Sports, Science and Technology of Japan (MEXT).

References

[1] Takano, H., K. Nishihara, *Prog. Nucl. Energ.*, 40, 473 (2002).

[2] Wallenius, J., *J. Nucl. Mater.*, 320, 142 (2003).

[3] Minato, K., M. Akabori, M. Takano, *et al.*, *J. Nucl. Mater.*, 320, 18 (2003).

[4] Hayes, S.L., J.K. Thomas, K.L. Peddicord, *J. Nucl. Mater.*, 171, 262 (1990).

[5] Aldred, A.T., B.D. Dunlap, A.R. Harvey, *et al.*, *Phys. Rev.*, B 9, 3766 (1974).

[6] Benedict, U., C. Dufour, O. Scholten, *J. Nucl. Mater.*, 73, 208 (1978).

[7] Takano, M., M. Akabori, Y. Arai, *et al.*, *J. Nucl. Mater.* 376, 114 (2008).

[8] Takano, M., M. Akabori, Y. Arai, *et al.*, "Thermal Expansion of TRU Nitride Solid Solutions as Fuel Materials for Transmutation of Minor Actinides", *J. Nucl. Mater.*, forthcoming.

[9] Suzuki, Y., Y. Arai, Y. Okamoto, *et al.*, *J. Nucl. Sci. Technol.*, 31, 677 (1994).

[10] Muromura, T., *J. Nucl. Sci. Technol.*, 19, 852 (1982).

[11] Damien, D.A., R.G. Haire, C.R. Peterson, *Techniques of Preparation and Crystal Chemistry of Transuranic Chalcogenides and Pnictides*, CONF 780823-8 (1978).

[12] Smirnov, V.S., V.V. Kosukhin, V.I. Minashkin, *Izv. Akad. Nauk. SSSR Neorg. Mater.*, 27, 2565 (1991).

[13] Martin, D.G., *J. Nucl. Mater.*, 152, 94 (1988).

Americium redistribution in irradiated (Am,Np,Pu,U)O_{2-x} fuels for fast reactors

Koji Maeda[1]**, Shinji Sasaki**[1]**, Fumiaki Kono**[1]**, Masato Kato**[2]**, Yoshiyuki Kihara**[2]
[1]Oarai Research and Development Center, Japan Atomic Energy Agency
[2]Nuclear Fuel Cycle Engineering Research Institute, Japan Atomic Energy Agency

Abstract

A uranium and plutonium mixed-oxide containing minor actinides (MA-MOX) fuel irradiation experiment (Am-1) is being conducted using the experimental fast reactor JOYO of the Japan Atomic Energy Agency. The objective of the experiment is to research early thermal behaviour of MA-MOX fuel such as restructuring and redistribution of minor actinides. The test results are expected to reduce the margins of the thermal design for MA-MOX fuel. Three MA-MOX fuel pins containing 2% neptunium and 2% americium (Np-Am-MOX) were supplied for two short-term irradiation tests in the Am-1. After the tests, non-destructive and destructive PIE were conducted. In particular, attention was paid to electron probe micro analyser (EPMA) measurements of the radial distribution of actinides. Both Am and Pu showed similar behaviour in the radial redistribution. Slight changes in the radial distribution of Np were observed. The degree of Am enrichment around the central void showed the dependence on initial fuel O/M ratio and Am was abruptly increased in the region of fuel temperatures above 2 200℃ after fuel restructuring.

Introduction

In the present nuclear fuel cycle, the minor actinides (MA) which have been generated in light water reactors (LWR) remain in the high-level radioactive waste. The long-term geological disposal of this waste may affect the environment. In order to reduce this environmental concern, separation of MA by waste reprocessing and their transmutation in reactors should be technically established. One of the options for combining techniques for the transmutation is to irradiate U and Pu mixed-oxide (MOX) fuel containing some MA (MA-MOX fuel) in fast reactors (FR). Based on a possible nuclear fuel cycle strategy, it has been proposed that the MA such as Np and Am produced from LWR are burnt as a 5%MA-MOX fuel in FR [1]. However, the designing of MA-MOX fuel still involves large uncertainties because published data on their thermal and mechanical properties are limited. In order to lessen the uncertainties, a MA-MOX fuel irradiation experiment (Am-1) [2] is being conducted using the experimental FR JOYO. This irradiation experiment is divided into a short-term phase to research the early thermal behaviour of MA-MOX fuel and a long-term phase to research the fuel burn-up dependant irradiation behaviour. In this irradiation programme, $(Am,Np,Pu,U)O_{2-x}$ fuel and $(Am,Pu,U)O_{2-x}$ fuel as representative MA-MOX fuels have been utilised. This paper describes the electron probe micro analyser (EPMA) results of redistribution of Am for $(Am,Np,Pu,U)O_{2-x}$ fuel used in the short-term irradiation tests. The Am-1 is one of the R&D tasks in the Fast Reactor Cycle Technology Development (FaCT) project. Some of the results have indicated that the thermal design for the $(Am,Np,Pu,U)O_{2-x}$ fuel has sufficient safety margins. The redistribution behaviour at a high linear heat rating (430 Wcm^{-1}) obtained from the short-term tests will be used to verify the thermal performance of the $(Am,Np,Pu,U)O_{2-x}$ fuel modelled in fuel pin thermal analysis codes.

Experimental

Fuel specimens

The pellets were fabricated in a normal alpha particle-tight glove box facility at the Nuclear Fuel Cycle Engineering Research Institute. The grid spaced fuel pins were separately loaded in the irradiation vehicle at the Oarai Research and Development Center. Fuel specifications of MA-containing MOX fuel are summarised in Table 1.

Table 1: Fuel specifications and irradiation conditions

Irradiation test	Fuel pin ID	Specimen position z/L	Fuel						Irradiation conditions		
			Am content (wt%)	Np content (wt%)	Fuel density (%TD)	O/M	Pu content (wt%)	Diameter (mm)	Local burnup (at%)	Linear heating rate (W/cm)	Cladding inner temperature (°C)
B11(1)	P506	0.50	2.0	2.0	93	1.98	28.80	5.42	0.0082	427	595
B11(2)	P604	0.50	2.0	2.0	93	1.98	28.80	5.42	0.0369	432	571
		0.54							0.0370	432	577
B11(2)	P605	0.50	2.0	2.0	93	1.95	28.80	5.42	0.0256	429	570
		0.54							0.0256	429	577

The nominal compositions of the $(Am,Np,Pu,U)O_{2-x}$ fuel were $(Am_{0.02},Np_{0.02},Pu_{0.29},U_{0.67})O_{2-x}$. The two O/M ratios which are expressed by subtracting the stoichiometry parameter x from 2, were chosen as 1.95 (low) and 1.98 (high). The fuel pellet diameter was 5.42 mm and pellet height was 8 mm. The fuel density was 93% theoretical density. Enrichments of ^{235}U and Pu were 8.3 and 30 wt.%, respectively.

The fuel pellets were inserted into the cladding tubes of 20% cold worked PNC-316 along with insulator pellets, a spring, etc. The cladding tube diameter and its wall thickness were 6.5 and 0.47 mm, respectively. The length of the fissile column was 200 mm. The $(Am,Np,Pu,U)O_{2-x}$ fuel pellets were loaded into the middle part of the fissile column and normal conventional MOX fuel pellets were loaded into the rest of the fissile column. The $(Am,Np,Pu,U)O_{2-x}$ fissile column length differed in the B11(1) and B11(2) tests, being 40 mm (z/L: 0.4 to 0.6) and 72 mm (z/L: 0.32 to 0.68), respectively. Here, z and L signify the distance from the bottom of the fissile column to an axial position and the fissile column length, respectively.

Short-term irradiation tests

In the Am-1 experiment, two short-term irradiation tests were conducted as follows. In the B11(1) test, the reactor power was held for 10 min at the maximum reactor power level, then the reactor experienced rapid shutdown by manual scram in order to preserve the fuel microstructure and to prevent additional fuel restructuring. In the B11(2) test, the reactor power was raised just as in the B11(1) test, and then the reactor was held at the maximum power level for 24 h, after which the shutdown by normal operation was carried out. Maximum local burn-up achieved was less than 0.0083 at.%. The maximum reactor power level corresponded approximately to a linear heat rating of 430 Wcm^{-1} [2]. Three fuel pins were irradiated at the maximum linear heating rate of 430 Wcm^{-1} and then all fuel pins were examined in detail.

Post-irradiation examinations

After the irradiation, non-destructive and destructive PIE were conducted. Fuel specimens were removed from the central part of the fissile columns for metallographic examinations with an optical microscope (OM). Then the elemental distributions of fuel constituents were examined in the specimens.

Quantitative analysis of the fuel with various compositions was done with the gamma shielded EPMA. The following parameters were selected for the analysis: working voltage, 20 kV; beam current for point analysis, 50 nA; use of a PET diffracting crystal. U, Np and Am were analysed with the M_α of their characteristic X-ray lines. Pu was analysed with the M_β line, and the intensity of the Pu M_β line was corrected by taking into consideration the overlap with the U M_β line. A 1%Am-MOX standard was used for the Am and Pu analysis. The peripheral region of the irradiated 2%Am-2%Np-MOX in the B11(1) test was used as a standard for the Np analysis. Radial concentration profiles were obtained by point analysis along the fuel radius. The measurements were done at points which avoided pores and fuel cracks.

Evaluation model of fuel radial temperature distribution

In order to estimate the fuel radial temperature distributions of each specimen, one-dimensional heat flow analysis was conducted using a FORTRAN program developed in JAEA [3]. In the analysis, the fuel restructuring was simplified into three regions (peripheral region, equiaxed region and columnar grain region). For the 10 minute-irradiated pins [B11(1)], however, a two-region model (peripheral region and columnar grain region) was adopted because equiaxed regions were not observed from ceramographs of these pins. The dimensional data of restructured region radii, central void radii, pellet outer radii and cladding inner/outer radii were measured in each ceramograph.

As for the fuel thermal properties, the experimental data such as thermal conductivity, melting point and so on of MOX fuel with low Am content has recently been examined in JAEA [4]. In the analysis, the thermal conductivity model, which includes the dependency of Am content, was used. Effect of Np was tentatively assumed to be the same as that of Pu, and the redistribution phenomena of Pu and Am were not considered in the fuel thermal conductivity. For a heat transfer model across the fuel-to-cladding gap, the model, which was evaluated based on the above experimental data (thermal conductivity and melting point) and power-to-melt tests in JOYO, was tentatively applied.

Evaluation model of redistribution of Am by pore migrations

The redistribution process of vapour transport and thermal diffusion lead to an enrichment of Pu around the central void in hypostoichiometric MOX fuels. However redistribution of Am has not been fully understood yet. Since the two short-term irradiation tests were conducted in a very short period of 24 h, Am redistribution by vapour transport was considered using the temperature distribution and pore migration model during fuel restructuring. The models of Pu redistribution by vapour transport have been published in the literature [5-8]. The mass transport equation for the radial redistribution of a concentration c is given in [8] as:

$$\partial c / \partial t = -\nabla \cdot J$$

where J and t are the mass current and time, respectively.

The porosity P equation is given:

$$\frac{\partial P}{\partial t} = \frac{1}{r}\frac{\partial}{\partial r}(r\upsilon P)$$

where υ is the porosity velocity.

Macroscopic current J, which is the movement of lenticular pores, is given:

$$J_r = -\frac{\overline{D}}{d\upsilon(r)}\delta c P_0 \frac{r_1}{r}\frac{\partial r_1}{\partial t}\exp\left(-\frac{\overline{D}}{l\upsilon(r)}\right)$$

where l and d are the pore diameter and thickness, respectively; P_0 is the initial porosity, $\overline{D}$ is a mean value of the diffusivity, and δc is Pu enhancement across the pore**.** In addition, $\overline{D}$ is expressed as follows:

$$\frac{\overline{D}}{\upsilon} = \frac{D_0}{4220l\left|dT/dr\right|}\exp\left[\left(66490 - \frac{E^*}{R}\right)/T\right],\ D = D_0\exp\left(-E^*/RT\right)$$

There has been only one paper on the diffusion of Am in UO_2 fuel, and the diffusion functions shown in that paper was used D_0 = 0.02 cm²/sec and E^* = 92 kcal/mol for fuel with O/M = 1.98 in this study [9].

Results and discussions

There were no indications of fuel melting in the X-ray computer tomography and radiography observations. The fuel pin was then sectioned for ceramography. Specimens were removed from the positions at $z/L = 0.50$ (axial core midplane) and $z/L = 0.54$ (maximum fuel centreline temperature). Irradiation conditions and fuel temperature of the specimens are summarised in Table 1.

Figure 1 shows ceramographs obtained for the fuel pins removed after the B11(1) and B11(2) tests. Fuel restructuring had already started within the brief 10 min irradiation, but no apparent fuel melting was observed. In the restructured region of the fuel with O/M ratio of 1.98, columnar grains were completely developed, and the central voids which were about 1 mm in diameter were formed. In the restructured region of the fuel with O/M ratio of 1.95, some of the lenticular voids were still migrating towards the central region, and the columnar grains were not completely developed yet. Comparing the (Am,Np,Pu,U)O_{2-x} fuel samples which had different fuel O/M ratios of 1.95 and 1.98, showed slight differences in the diameters of the columnar grains and the central void, respectively. This suggested that the test parameter of fuel O/M ratio had little influence on fuel restructuring behaviour.

The radial intensity profiles of Am, Np and Pu for the specimens ($z/L = 0.50$) of both the B11(1) and B11(2) tests are shown in Figures 2(a) and 2(b), respectively. The intensity profile of Np was almost flat in the B11(1) test, and after the B11(2) test. Thus the profile of Np in the fuel was still flat even after fuel restructuring. In contrast, Pu and Am were slightly redistributed in the columnar grains region after the B11(1) test, and then Pu and Am intensities increased toward the central void and were significantly redistributed in the columnar grains region during the B11(2) test. These intensity profiles of Am and Pu were similarly distributed as a function of fuel radius. To the contrary, intensity of U decreased towards the central void. This was attributed to vapour transport of uranium as UO_3 down the radial temperature gradient during the irradiation [10]

Distributions of Am amount and fuel temperature for the specimens used in the B11(1) and B11(2) tests are shown in Figures 3 through 5. Radial distributions of Am amount in the fuel specimens with O/M ratios of 1.98 and 1.95 were similar up to 1.8 mm from the fuel surface. But the enrichment of Am near the central void became larger in the specimens with O/M ratio of 1.98. Additionally, the degree of redistribution of Am in the specimens with O/M ratio of 1.95 was smaller than that of fuel with O/M ratio of 1.98. This was attributed to less vapour transport of uranium as UO_3, which was due to the low oxygen potential of fuel with O/M ratio of 1.95. A similar dependence of O/M ratio on radial distribution of Pu was also seen in the specimens. In this low oxygen potential condition due to the initial O/M ratio of 1.95, the radial profiles of Am and Pu also showed a similar tendency to redistribute in the columnar grains region. This was attributed to the O/M dependence on the vapour transport of uranium as UO_3 down the radial temperature gradient during the B11(2) test. The maximum enrichment of Am less than 3.5 wt.% was detected in the specimen with O/M ratio of 1.98 ($z/L = 0.50$). Increases of the elements were found to be sufficiently low enough to suggest larger safety margins can be used in thermal design of the fuel pins.

Distributions of Am amount as a function of fuel temperature in the specimens used in the B11(1) and B11(2) tests are shown in Figures 7 and 8. Enrichments of Am near the central void in the specimens with O/M ratios of 1.98 and 1.95 were sharply increased for fuel temperatures of more than 2 200°C and 2 250°C, respectively. In this narrow high temperature region coarse grains developed and a number of lenticular voids were coalesced as shown in Figure 9. This suggested that the radial limit of void migration was taken to correspond to the narrow region in which the rates decreased to an insignificant value. In the columnar grain region, the amount of Am increased with the increase of fuel temperature towards the fuel centre. These results revealed that the radial movement of lenticular voids contributed to vapour transport of Am to the fuel centre. Profiles of Am in the fuel with O/M ratio of 1.95 were similar to those of the fuel with O/M ratio of 1.98. But the degree of the redistribution of Am was smaller than that of fuel with O/M ratio of 1.98. Similar behaviour of Pu is known and it is attributed to less vapour transport of U as UO_3, which is due to the low oxygen potential of fuel with low O/M ratio. It seemed that under low oxygen potential with O/M ratio of 1.95, the radial profiles of Am also showed a similar tendency to Pu to redistribute in the columnar grains region.

Radial redistribution of Am concentration was calculated and compared to the results of the EPMA analysis for the specimens with O/M ratio of 1.98 used in the B11(2) test. The results are shown in Figure 10. In comparison with the results of EPMA analysis, it was found that Am redistribution was reasonably calculated by using the pore migration model. This suggested that the Am redistribution near the central void became significant within a comparatively brief irradiation period and the redistribution was dominated by the mechanism of vapour transport.

Summary

In the (Am,Np,Pu,U)O_{2-x} fuel, Am and Pu increased moving toward the fuel centre and their radial intensity profiles were similar. These radial profiles of Am and Pu indicated that the elements had a similar tendency to redistribute in the columnar grains region and the degree of enrichments near the central void had a dependency on fuel O/M ratio. Radial redistribution of Am concentration was calculated and compared to the results of the EPMA analysis. It was found that Am redistribution was reasonably calculated by using the pore migration model. This suggested that the Am redistribution near the central void became significant within a comparatively brief irradiation period. The results pointed to the dominant mechanism of the redistribution being vapour transport.

Acknowledgements

The authors wish to gratefully acknowledge the contributions of Y. Ohsato, Y. Onuma and S. Nukaga (Nuclear Technology and Engineering Corporation) for conducting the destructive PIE.

References

[1] Ichimiya, M., T. Mizuno, M. Konomura, *Proceedings of GLOBAL 2003*, New Orleans, Louisiana, USA, 16-20 November 2003 (CD-ROM).

[2] Sekine, T., *et al.*, *Proceedings of GLOBAL 2007*, Boise, Idaho, USA, 9-13 September 2007 (CD-ROM).

[3] Inoue, M., *et al.*, *J. Nucl. Mater.*, 326, 59-73 (2004).

[4] Kato, M., *et al. Evaluation of Thermal Physical Properties for Fast Reactor Fuel – Melting Point and Thermal Conductivities*, JAEA-Technology 2006-049 (2006) (in Japanese).

[5] Bober, M., C. Sari, G. Schumacher, *J. Nucl. Mater.* 39, 265-284 (1971).

[6] Meyer, R.O., *J. Nucl. Mater.*, 50, 11-24 (1974).

[7] Olander, D.R., *J. Nucl. Mater.*, 49, 35-44 (1973).

[8] Clement, C.F., M.W. Finnis, *J. Nucl. Mater.*, 75, 193-200 (1978).

[9] Schmitz, F., R. Lindner, *J. Nucl. Mater.*, 17, p. 259 (1965).

[10] Rand, M.H., T.L. Markin, *Thermodynamics of Nuclear Materials 1967, Proceedings of the IAEA Symposium*, Vienna (1968), p. 637.

Figure 1: Ceramographs of fuel pins used in the Am-1 experiment

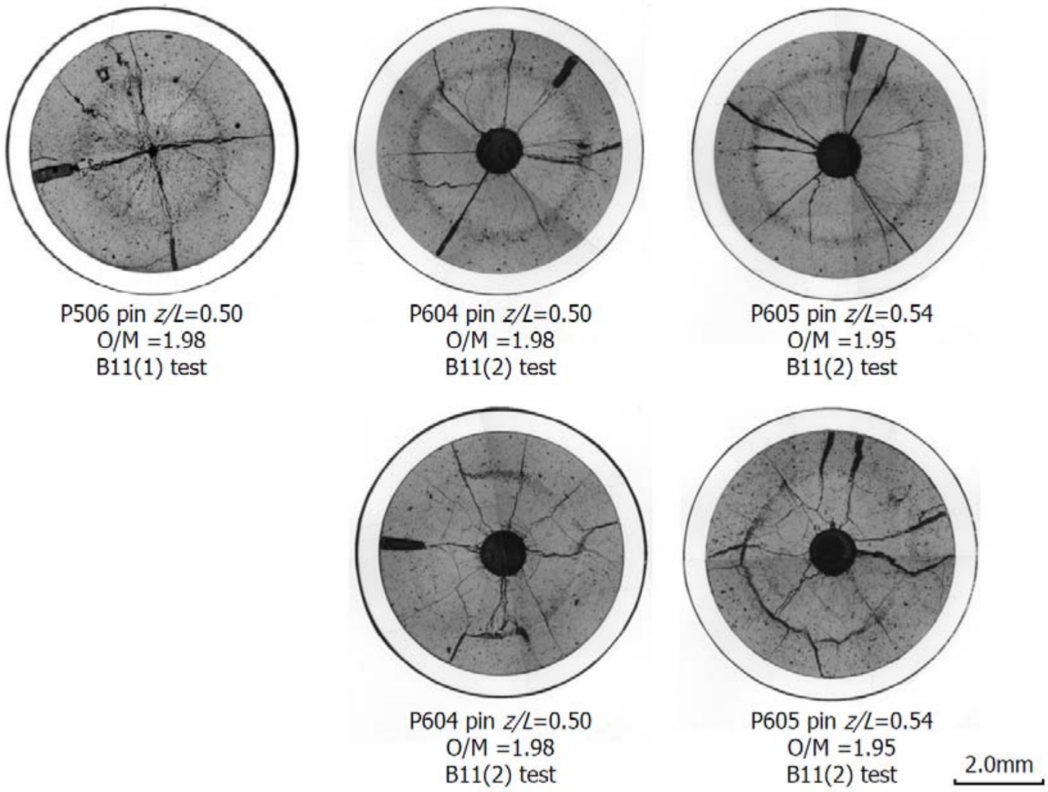

P506 pin z/L=0.50
O/M =1.98
B11(1) test

P604 pin z/L=0.50
O/M =1.98
B11(2) test

P605 pin z/L=0.54
O/M =1.95
B11(2) test

P604 pin z/L=0.50
O/M =1.98
B11(2) test

P605 pin z/L=0.54
O/M =1.95
B11(2) test

Figure 2: Radial intensity profiles of Np, Am and Pu in the specimens

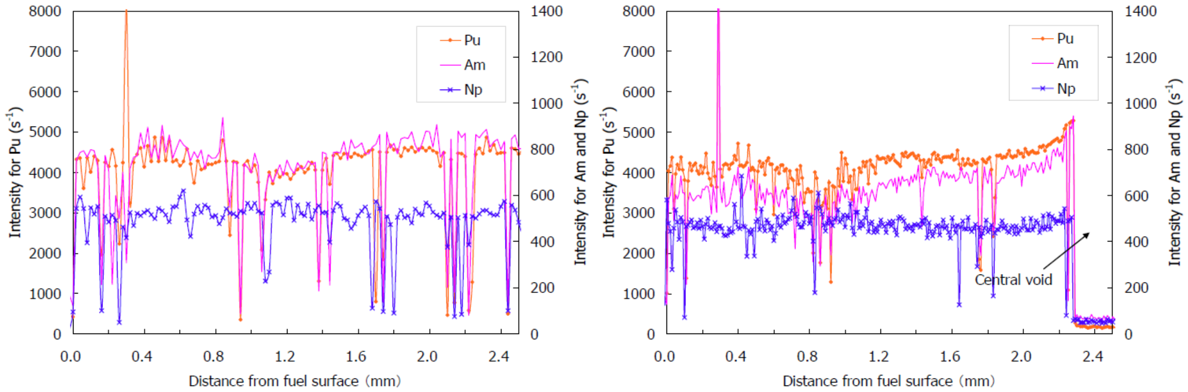

(a) First test, P506 pin *z*/*L*=0.50 (b) Second test, P604 pin *z*/*L*=0.50

Figure 3: Distribution of Am and fuel temperature [B11(1), P506 pin]

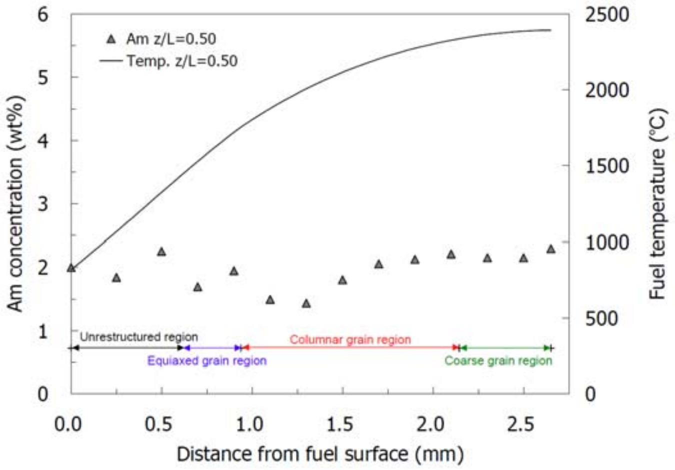

Figure 4: Distribution of Am and fuel temperature [B11(2), P604 pin]

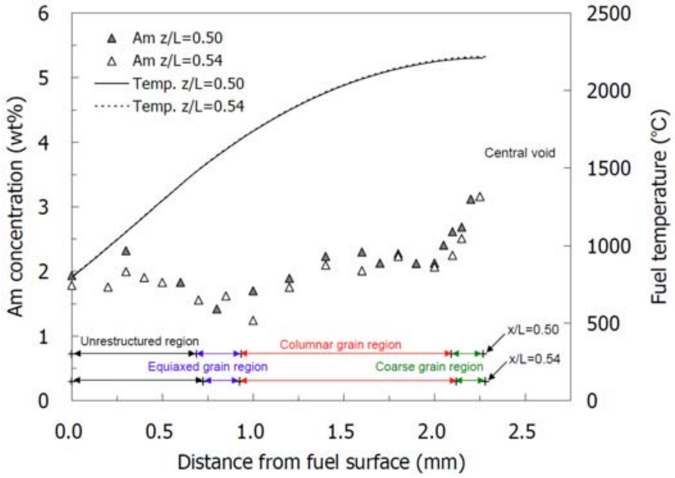

Figure 5: Distribution of Am and fuel temperature [B11(2), P605 pin]

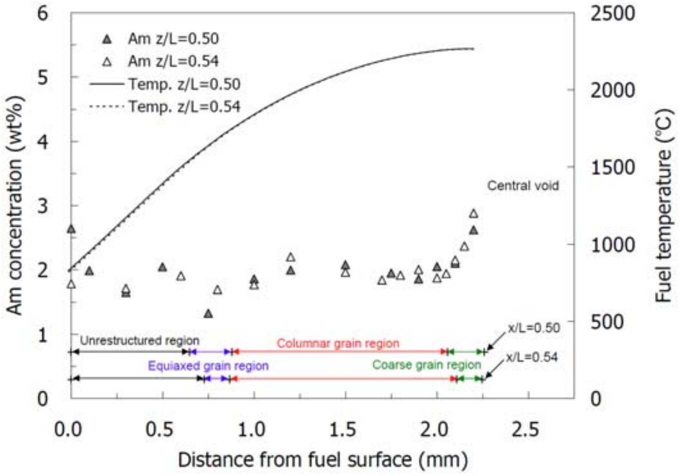

Figure 6: Distribution of Am as a function of fuel temperature [B11(1), P506 pin]

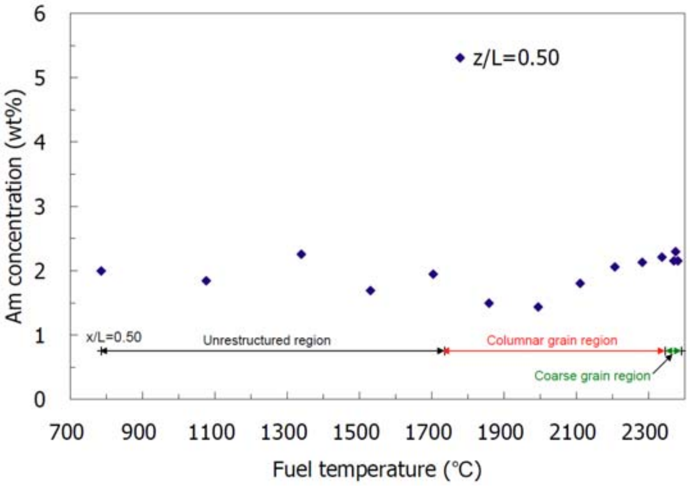

Figure 7: Distribution of Am as a function of fuel temperature [B11(2), P604 pin]

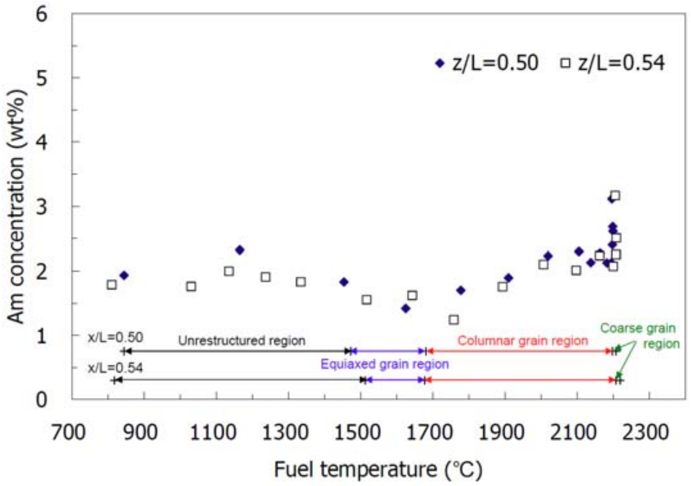

Figure 8: Distribution of Am as a function of fuel temperature [B11(2), P605 pin]

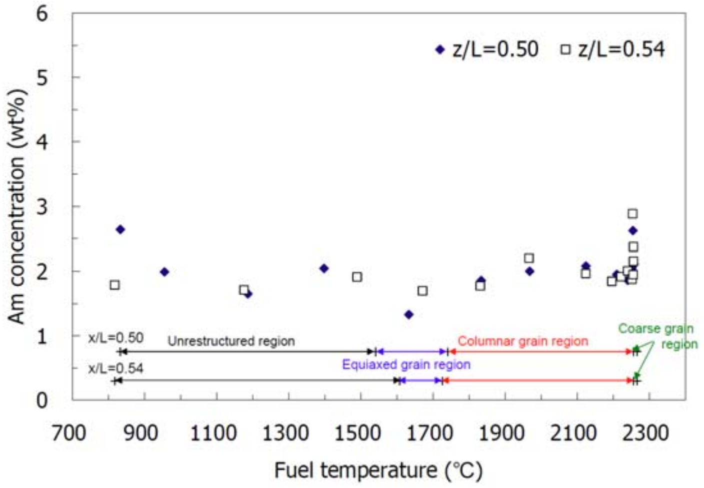

Figure 9: Enlarged ceramograph around central void [B11(2), z/L = 0.50, P506 pin]

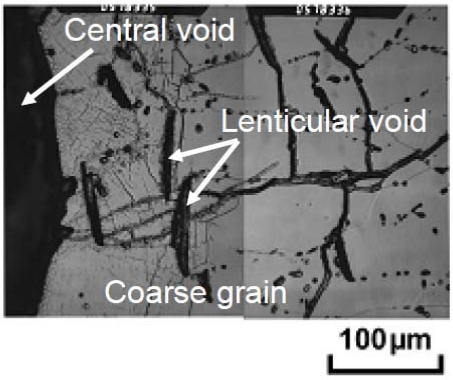

Figure 10: Comparison of Am distributions for EPMA analysis and calculated results